Global scale patterns and trends in tropospheric NO$_2$ concentrations

Daniel Klingmyr

Daniel Klingmyr (2019). Global scale patterns and trends in tropospheric NO$_2$ concentrations.
Master degree thesis, 30/ credits in Master in Geographical Information Science
Department of Physical Geography and Ecosystem Science, Lund University

Global scale patterns and trends in tropospheric NO$_2$ concentrations

Daniel Klingmyr
Master thesis, 30 credits, in Geographical Information Sciences

Supervisors: Torbern Tagesson and Sadegh Jamali
Department of Physical Geography and Ecosystems Science, Lund
University

Preface

I would like to thank my excellent supervisors Torbern Tagesson and Sadegh Jamali for your support, knowledge and patience throughout the work with this thesis. Your feedback and guidance inspired me to work harder and motivated me to keep going when things got difficult. Thank you for helping me finish this thesis.

Abstract

Nitrogen dioxide (NO_2) is an important air pollutant with both environmental and epidemiological effects. The main aim of this thesis is to explore spatial patterns and temporal trends of tropospheric NO_2 concentrations globally using data from the OMI instrument aboard NASA's Aura spacecraft. Additional aims are to validate the satellite data by comparing it to ground-based measurements, and to find the timing and magnitude of the most significant breakpoints over the study period of 2005 through 2018. The results show that there was statistically significant agreement between the satellite-based and ground-based datasets (r = 0.53). The global trend over the study period was negative (- 0.41 molecules cm^{-2} y^{-1}), but a large difference was found between land and oceans (trends of - 1.84 molecules cm^{-2} y^{-1} and 0.35 molecules cm^{-2} y^{-1}, respectively). USA, western Europe, India, China and Japan were identified as hotspot areas with high NO_2 concentrations, while all these areas had negative trends over the study period. Finally, it was found that the year 2008 had the highest number of significant breakpoints, out of which almost all were negative.

Table of contents

List of figures

List of tables

List of abbreviations

A	AMF	Air mass factor
B	BrO	Bromine monoxide
C		
D	DBEST	Detecting Breakpoints and Estimating Segments in Trend
	DOAS	Differential optical absorption spectroscopy
	DOMINO	Derivation of OMI Tropospheric NO_2
E	EOS	Earth Observing System
F		
G	GOME	Global ozone monitoring experiment
H	HCHO	Formaldehyde
	HIRDLS	High-Resolution Dynamics Limb Sounder
I		
J		
K		
L		
M	MLS	Microwave Limb Sounder
N	NASA	National Aeronautics and Space Administration
	NO	Nitric oxide
	NO_2	Nitrogen dioxide
O	O_3	Ozone
	OH	Hydroxide
P		
Q		
R	RMSE	Root mean square error
S	SCD	Slant column density
	SCIAMACHY	Scanning imaging absorption spectrometer for atmospheric chartography
	SO_2	Sulfur dioxide
T	TROPOMI	Tropospheric monitoring instrument
U	UV	Ultraviolet
V	VCD	Vertical column density
	VIS	Visible

1. Introduction

Air pollution is one of the main threats to human health, ecosystems and climate on a global scale (Paraschiv et al., 2017; Bechle et al., 2013). The global population is growing substantially and more than half of the world's population now live in urban areas. Large urban areas and high population densities are hotspots for air pollution (Paraschiv et al., 2017; Schneider et al., 2015). According to the World Health Organization (WHO), about 3 million people die annually due to ambient air pollution, mainly in low- and middle-income countries, and about 90 % of the world's population are exposed to air that exceed the WHO air quality guidelines (WHO, 2016).

Nitrogen dioxide (NO_2) is one of the most important air pollutants in the atmosphere (Georgoulias et al., 2019) and has been linked to a number of both environmental and epidemiological effects (Streets et al., 2013; Bechle et al., 2013). It is formed in processes where nitrogen reacts with oxygen in high temperatures, e.g. through lightning and the combustion of fuels (Zhang et al., 2017). The main anthropogenic sources of NO_2 emissions are transport, industry processes and energy production (Liu et al., 2016). Some of the main environmental effects that are linked to high NO_2 concentrations are acidification, eutrophication and photochemical formation of ozone (O_3) (Zhang et al., 2018; Zhang et al., 2017; Streets et al., 2013). NO_2 also modifies the radiative balance in the atmosphere and influences the atmospheric lifetime of greenhouse gases (Geourgoulias et al., 2019; Boersma et al., 2011). NO_2 is toxic at high concentrations and the epidemiological effects include respiratory illnesses such as lung cancer, asthma exacerbations and cardiopulmonary mortality (Georgoulias et al., 2019; Zhang et al., 2017; Bechle et al., 2013; Ordóñez et al., 2006). NO_2 has a short atmospheric lifetime, on average 3.8 ± 1.0 hours (mean $\pm$ 1 standard deviation) (Liu et al., 2016) as it reacts with sunlight which triggers the production of OH (Safieddine et al., 2013). Therefore, high concentrations of tropospheric NO_2 is mainly confined to its emission sources, which in general are urban and industrialised areas (Georgoulias et al., 2019; Bechle et al., 2013).

Monitoring of NO_2 concentrations and other air pollutants can be done with ground-based monitoring stations. However, monitoring stations tend to be clustered in city centres, have a small spatial coverage and are often lacking in developing countries (Yu et al., 2018; Bechle et al., 2013). Ground-based air quality monitoring is thereby unevenly distributed, and leave large areas under-represented (Lamsal et al., 2015; Yu et al., 2018). An alternative approach to monitor air pollution is the usage of remotely sensed satellite data which increase the spatial coverage. Major advances have been made over the past decades to use satellite-based instruments to monitor atmospheric pollutants (Paraschiv et al., 2017). Satellite-based monitoring of NO_2 started in 1995 with the Global Ozone Monitoring Experiment (GOME) instrument (Schneider et al., 2015). Since then, other satellite-based instruments have been used to monitor tropospheric NO_2, such as GOME-2, the Scanning Imaging Absorption spectroMeter for Atmospheric CHartographY (SCIAMACHY), the Ozone Monitoring Instrument (OMI), and the recent TROPOspheric Monitoring Instrument (TROPOMI) aboard Sentinel-5. Out of these instruments, OMI offers the longest continuous monitoring record (ongoing since 2004) and has a relatively high spatial resolution (13

* 24 km^2 at nadir) (Zhang et al., 2017; Streets et al., 2013). Potential errors in estimating NO$_2$ concentrations from satellite data include uncertainties in surface albedo, aerosols, cloud parameters, slant column density and air mass factor calculations (Bechle et al., 2013; Streets et al., 2013; Boersma et al., 2011). Therefore, for satellite-based measurements to be trustworthy, the data needs to be validated against ground-based monitoring stations (McPeters et al., 2008).

Studies of long-term trends provides information on changes in air pollution, distribution patterns, and is useful to assess the effects of emission mitigation efforts (Wang & Wang, 2018; Geddes et al., 2016; Munir et al., 2013). Studies that investigate NO$_2$ trends using OMI data and validated the results against ground-based measurements have been performed previously. For instance, Lamsal et al. (2015), Zu et al. (2015), Tong et al. (2015) and Bechle et al. (2013) did studies in the U.S., de Foy et al. (2016) studied NO$_2$ trends over China, Gruzdev and Elokhov (2010) in Russia, Paraschiv et al. (2017) in eight European cities and Duncan et al. (2016) in cities around the globe. These studies have overall found declining NO$_2$ trends in their respective study areas and good agreement between OMI and ground-based measurements with correlation coefficients ranging between 0.3 – 0.93. NO$_2$ trend studies on a global scale have also been performed previously using various satellite sensors. Georgoulias et al. (2019) used GOME, GOME-2 and SCIAMACHY to study trends from 1996 – 2017, Krotkov et al. (2016) used OMI to study trends between 2005 – 2015, Geddes et al. (2016) used GOME, GOME-2 and SCIAMACHY between 1996 – 2012, Miyazaki et al. (2017) used OMI, GOME-2 and SCIAMACHY between 2005 – 2014 and Schneider et al. (2012) used SCIAMACHY between 2002 – 2011. These studies have overall found both negative and positive regional trends.

In this study, data from OMI will be used to study global and regional patterns and trends in tropospheric NO$_2$ concentrations from 2005 to 2018, thereby contributing to the research in spatiotemporal patterns in NO$_2$ concentrations by updating and expanding the work done by previous scholars. Furthermore, linear- and non-linear trend types as well as timing and magnitude of the major breakpoints will be spatially explicit analysed at global scale.

1.1. Overall aim and research questions

The aim of this study is to map the spatial patterns and temporal trends of global tropospheric NO_2 concentrations from 2005 to 2018, using data from the OMI instrument. A second aim is to validate the OMI data by analysing whether the satellite-based measurements are correlated with in situ data from ground-based monitoring stations. A third aim is to analyse if regional differences can be found in global NO_2 concentrations and if any significant temporal trends exist over the study period. Finally, timing and magnitude of significant breakpoints of NO_2 concentrations will be analysed for each grid cell on a global scale.

Research questions to be responded in this thesis are:
- How does the OMI data compare to the ground-based measurements?
- Based on the satellite data, do we see any spatial patterns in NO_2 concentrations globally?
- Do we see any temporal trends in the concentrations of NO_2 over the study period?
- And finally, when did the most significant breakpoint events occur?

Page intentionally left blank.

2. Background

2.1. The Aura spacecraft

Aura is one of the National Aeronautics and Space Administration's (NASA) Earth Observing System (EOS) satellites. It was launched in 2004 with the mission to collect data of global air pollution and to monitor the chemistry and dynamics of Earth's atmosphere on a daily basis (NASA, 2007). Aura follows a sun-synchronous near polar orbit at an average height of 705 km and has a 16-day repeat cycle. The satellite has an orbital period of approximately 99 minutes and an Equator overpass time of 13:45 (± 15 min) local time (Goldberg et al., 2019; Bucsela et al., 2013; OMI team, 2012).

Aboard Aura there are four instruments; the High-Resolution Dynamics Limb Sounder (HIRDLS), the Microwave Limb Sounder (MLS), the Tropospheric Emission Spectrometer (TES), and the Ozone Monitoring Instrument (OMI) (NASA, 2007; Levelt & Noordhoek, 2002). In this study, data collected with the OMI instrument has been used.

2.2. OMI characteristics and instrument description

OMI is a nadir-looking push broom hyperspectral imaging spectrometer. It measures reflected solar radiation in the ultraviolet and the visible light (UV/VIS) channels of the electromagnetic spectrum (wavelength range of 264 – 504 nanometre (nm)) with a spectral resolution of 0.42 – 0.63 nm (Ziemke et al., 2017; Dobber et al., 2006). The instrument has a surface swath width of 2 600 km and achieves global coverage in about 14.5 orbits with a 13 * 24 km (along track * across track) field of view at nadir (Goldberg et al., 2019; Kim et al., 2018). The objective of OMI is to measure key air quality components and parameters at a high spatial and spectral resolution in order to study the recovery of the ozone layer, climate change and tropospheric air pollution (Dobber et al., 2006). The specific components and parameters that OMI measures are cloud pressure and coverage, aerosols, surface irradiance and total column and vertical profile of the trace gases ozone (O_3), nitrogen dioxide (NO_2), sulfur dioxide (SO_2), formaldehyde (HCHO), bromine monoxide (BrO) and chlorine dioxide (OClO) (Tan et al., 2018; Levelt & Noordhoek, 2002; Levelt et al., 2017).

The OMI instrument consists of three main elements; the optical assembly, the electronics unit and the interface adaptor module (Levelt & Noordhoek, 2002). In the optical assembly, the incoming light enters a telescope and is depolarised using a scrambler. The light is then split depending on wavelength into a UV or a VIS channel and is then focused by a mirror on to two separate detectors which converts the optical signal to an analogue electrical signal (Dobber et al., 2006; Levelt et al., 2017). The electrical signal is then transferred to the electronics unit which digitizes the signal to measurement data. Another function of the electronics unit is to control the settings of the optical assembly and to receive commands from the interface adaptor module. The digitized signal data is then sent from the electronics unit to the interface adaptor module, which is the interface between OMI and the Aura satellite (Dobber et al., 2006; Levelt & Noordhoek, 2002).

2.3. The OMI row anomaly

Since 2007, OMI has suffered from reduced quality and spatial coverage in parts of the sensor's field of views. This problem is dynamic, meaning that it has varied over time, and is referred to as a row anomaly (Tan et al., 2018; Torres et al., 2018; Krotkov et al., 2017). The reason for the row anomaly is not fully understood but is believed to be caused by a physical blockage of the optics from loosening fabric material on the interior walls of the sensor (Torres et al., 2018; Krotkov et al., 2017). However, this row anomaly only affects the level 1B and level 2 OMI products, which contain orbital swath data. The level 3 product is made up of composites that are produced by filtering out the affected data and averaging the unaffected pixels, thereby only maintaining data with 'optimal quality' (OMI team, 2012). In this study, the level 3 product was used.

2.4. OMI NO_2 retrieval

There are two OMI NO_2 products available; NASA's standard product and the Royal Netherlands Meteorological Institute's Derivation of OMI Tropospheric NO_2 (DOMINO) product. The difference between the two products is how they separate NO_2 in the stratospheric and tropospheric columns and their respective air mass factor (AMF) calculations (Ialongo et al., 2016). The AMF is defined as the ratio of the slant column to the vertical column (Palmer et al., 2001). The product that has been used for this study is the NASA standard product version 3.

The NO_2 retrieval of the NASA standard product algorithm has four main steps; obtaining the NO_2 slant column density (SCD), estimating the stratospheric contribution, calculating a tropospheric AMF and finally to use the SCD and AMF to calculate the vertical column density (VCD) (Hains et al., 2010; Bucsela et al., 2006). The SCD is the total amount of NO_2 (molecules cm^{-2}) observed from OMI through the atmosphere in an angled view, while the VCD is total amount in a vertical view. In order to retrieve the SCD, OMI uses differential optical absorption spectroscopy (DOAS) spectral fitting technique. NO_2 is measured in the wavelength range $405 - 465$ nm of the VIS and near-UV channels, where NO_2 has strong spectral absorption (Krotkov et al., 2017; Bucsela et al., 2006). This results in the total SCD, which includes both stratospheric and tropospheric NO_2. Since NO_2 in the stratospheric and tropospheric columns have different origins and vary in spatial distribution (Bucsela et al., 2006), there is a need to separate the two columns. In the NASA standard product, this is done using an algorithm which results in an interpolated stratospheric NO_2 mask (Tong et al., 2015). The tropospheric SCD is then derived by subtracting the contribution from the interpolated stratospheric NO_2 mask from the total SCD. Next, the AMF is calculated from an assumed NO_2 profile, cloud fraction and surface albedo (Tong et al., 2015; Boersma et al., 2011). Finally, the VCD, which is the final product and the variable of interest, is derived from dividing the SCD by the AMF (Krotkov et al., 2017; Bucsela et al., 2013).

2.5. Trend classification

Trend analysis is a statistical procedure of finding and extracting underlying patterns in time series data. In this study, Polytrend, an algorithm that accounts for non-linear change in a trend, was used (Jamali et al. 2014). It has a polynomial fitting-based scheme that divides trends into cubic, quadratic, linear, and concealed trend types. The scheme of the program consists of a 3-phase procedure. First, the fit of a cubic model (highest order polynomial considered) is tested by evaluating statistical significance of the fit (statistical significance level 0.05). If the test fails, the same procedure is applied to test the fit of a quadratic model. If the quadratic model test fails, a linear model is tested (Fig. 1).
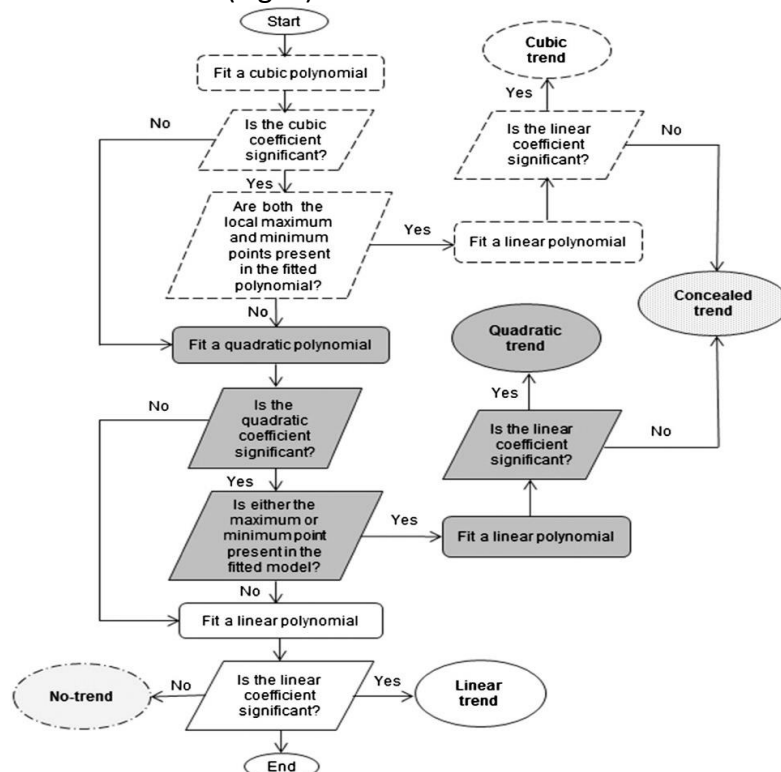
Figure 1. A schematic representation of the Polytrend workflow. Figure from Jamali et al. (2014).

There are five possible trend type outcomes in the output; cubic, quadratic, linear, concealed and no-trend. The cubic trend type means that the trend line of the cell has two or more bends, implying that the cell has experienced more than one direction change of its trend line over the study period (i.e. first negative, followed by positive and then negative again, or vice versa). The quadratic trend type is a trend line with one bend in its curve, implying that the cell has experienced one direction change of its trend line over the study period (i.e. first positive and then negative trend, or vice versa). The linear trend type means that the trend line has had a uniform direction over the study period (either positive or negative). The concealed trend type consists of cells with either cubic or quadratic trend types, but with no significant net change in NO_2 over the study period. Finally, the no-trend trend type consists of cells where all other trend models were statistically insignificant at the 0.05 significance level (Jamali et al., 2014). In this thesis, the algorithm was used to classify the type of trend each cell experienced and to find the slope direction, significance (significance level 0.05) and the slope coefficient of each cell's time series curve over the study period.

2.6. Breakpoint analysis

Detecting Breakpoints and Estimating Segments in Trend (DBEST) is a computer program for analysing time series of satellite sensor data. Its change detection algorithm detects trend changes (breakpoints), determines their type (abrupt or non-abrupt) and significance (significance level 0.05), and estimates timing and magnitude of the detected changes. This is done by using a segmentation algorithm and user-defined thresholds (Jamali et al. 2015). In DBEST, single time-step differences for all data points in the time series are calculated as follows:

Linear segments are computed for all points in the time series. A straight line is then fitted through each pair of successive start and end points. The point in the segment with the maximum distance to the line is then selected (Fig. 2 a). If this point is above a user-defined distance threshold value, these points are called breakpoints. The selected breakpoints are fitted to the time series and are treated as adjoining linear segments, which results in a time series made up of continuous trends composed of linear segments (Fig. 2 b). Depending on the number of changes that are of interest, the breakpoints are selected based on the magnitude of their trend local change. For a change to be considered as abrupt it needs to satisfy two criteria. First, the difference between two successive points needs to exceed the first level-shift threshold. Second, the magnitude of the change needs to be large enough to shift the mean by the second level-shift threshold over the period of the duration threshold. For a more thorough description of DBEST, see Jamali et al. (2015).
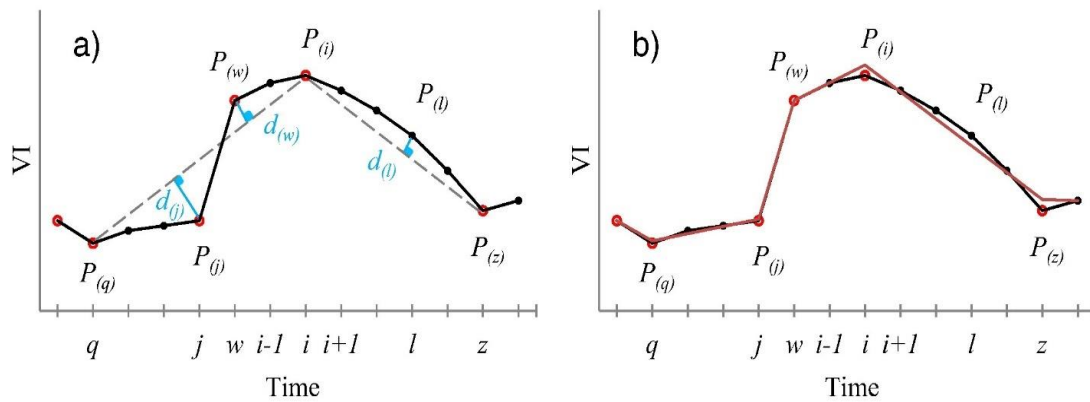
Figure 2. A schematic representation of the DBEST workflow for a time series, in this case for vegetation index (VI). (a) - Straight lines (dashed in grey) are fitted through consecutive peak and valley points and turning points (in red) are computed. (b) – Linear trends (segments in red) are then computed by the DBEST algorithm. Figure provided from Jamali et al. (2015).

The user-defined parameters of DBEST and the threshold values used in this study are as follows:

- First level-shift threshold: The lowest difference allowed in NO_2 concentrations between the level-shift point and the next data point. In this case, the lowest allowed NO_2 concentration difference was set to 2 molecules cm^{-2}.
- Second level-shift threshold: The lowest difference allowed in the means of the data calculated over the period before and after the level-shift point. In this case the lowest allowed difference was set to 10 molecules cm^{-2}.
- Duration threshold: The lowest time period (time steps) allowed within which the shift of the mean of the data level before and after the level-shift point persists; and the lowest spacing between successive level-shift points. In this case set to 2 years.
- Distance threshold: The lowest perpendicular distance allowed from the farthest point to the straight line between successive peak and valley points. In this case, the lowest distance allowed was set to 0.5 molecules cm^{-2}.
- Change number: The number of greatest changes (breakpoints) of interest for detection. In this case, the number of breakpoints to be detected was set to 1 in order to find the major change of each pixel over the study period.
- Change magnitude: The lowest magnitude of change allowed for detection. In this case set to 0.5 molecules cm^{-2}.
- Type: Either cyclical for time series with seasonal data or non-cyclical for time series without seasonal cycle (deseasonalized data). In this case non-cyclical.
- Period: The seasonality period value. In this case left empty since deseasonalized data was used.
- Algorithm: The algorithm used by DBEST, either 'generalization' or 'change detection'. In this case change detection.
- m: The number of changes or breakpoints of interest for detection. In this case set to 1 to find the major change over the study period.
- Alpha: The statistical significance level used for testing significance of detected changes. In this case 0.05.

Page intentionally left blank.

3. Data

3.1. Satellite-based NO$_2$ dataset

The NO$_2$ dataset is the OMI/Aura level 3 NO$_2$ (OMNO2d) version 3 standard product which was downloaded from NASA's Earth Observation data collection (Earthdata, 2019). The OMNO2d product contains composites of daily total tropospheric column NO$_2$ data with a spatial resolution of 0.25° * 0.25°. The data is stored in the version 5 EOS Hierarchical Data format (HE-5) (Krotkov et al., 2017). In this study, OMI data from January 1st of 2005 until December 31st of 2018 has been used. In total, 5 173 daily OMNO2d HE-5 files were used.

3.2. Ground-based NO$_2$ dataset

The ground-based data is monthly averages of daily observations (n = 1 706 830) and annual averages (n = 6 113) of atmospheric NO$_2$ concentrations from monitoring stations in the USA between the years 2005 to 2018 (Fig. 3), provided by the US Environmental Protection Agency (US EPA, 2019). The reference method used by the US EPA for collection of ambient NO$_2$ is chemiluminescence analysis (Gillam & Hall, 2016). This method is based on the reaction of nitric oxide (NO) with ozone (O$_3$). The principle of the method is that a sample of ambient gas enters a reaction chamber where NO molecules react with O$_3$ to form NO$_2$. The reaction produces a quantity of light, a phenomenon known as chemiluminescence. The intensity of the light, which is proportional to the concentration of NO$_2$, is then measured to determine the concentration of NO$_2$ (Gillam & Hall, 2016; US EPA, 2002).

3.3. Ancillary data

The ancillary data used in this study consist of a global shapefile with administrative boundaries on the country and continent levels, downloaded from the Database of Global Administrative Areas (GADM, 2018).
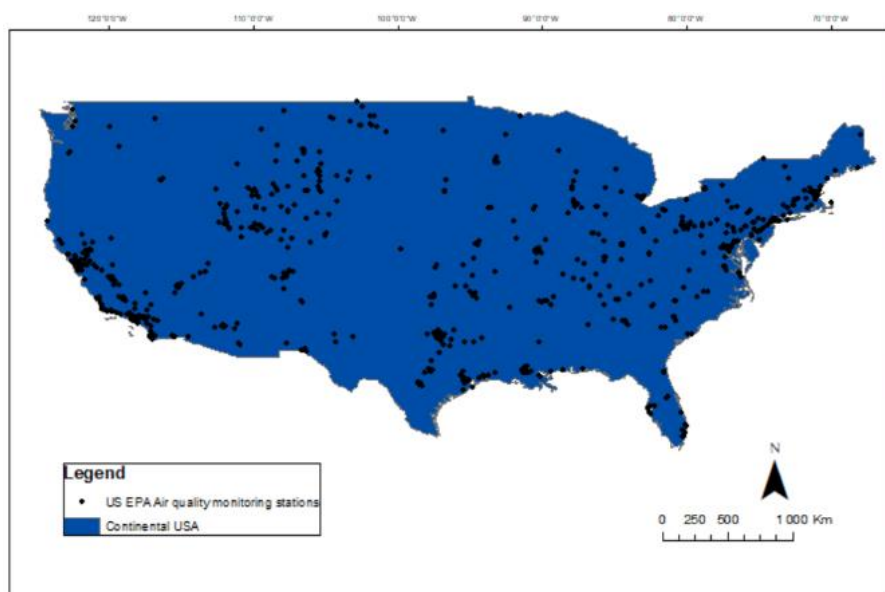
Figure 3. Spatial distribution of US EPA air quality monitoring stations used in this study.

Page intentionally left blank.

4. Methodology

4.1. Data validation

The OMNO2d files were averaged monthly and yearly. The averaged satellite-based NO_2 data was then compared to ground-based NO_2 data in order to verify the validity of OMNO2d data product. Data from the US EPA was chosen for the comparison. The choice was based on availability and usability of the data, as pre-generated files of annual summaries for monitoring station with associated coordinates for the full study period (2005 – 2018) were available.

Since the two datasets use different units (molecules cm^{-2} for the satellite-based data and ppb for the ground-based data), the values were recalculated to z-statistics using the following equation:

$$z = \frac{(x - \mu)}{\sigma}$$

Where
z = the resulting z-statistic
x = the original OMI or monitoring station value
μ = the mean value of the OMI or monitoring station data
σ = the standard deviation of the OMI or monitoring station data

Histograms were created to compare the shape and spread of the internal distributions of the z-scores from the satellite-based and the ground-based data. Then, ordinary least squares linear regressions, Pearson's correlation analyses and root mean square error (RMSE) was computed for the two datasets. The analyses were performed for all monthly and annual data points, the spatial averages of all annual data points, and the temporal averages of all annual data points.

4.2. Analysis of spatial patterns and temporal trends

The spatial patterns were analysed by averaging all OMI NO_2 data over the study period. For analysing the temporal trends, a time series of each year's mean NO_2 concentration was first calculated. Then, DBEST was used to analyse the timing and magnitude of greatest significant breakpoints while Polytrend was used to analyse the significant slope coefficient and trend types of each cell's time series of tropospheric NO_2 concentration over the study period.

Page intentionally left blank.

5. Results

5.1. Data validation

Differences between the z-scores of the ground-based and the satellite-based datasets were found (Fig. 4). The shape of the satellite-based data is bimodal while the shape of the ground-based data is unimodal and skewed to the right. Another difference between the datasets is the spread of the values. The range of the ground-based dataset is slightly higher than the range of the satellite-based dataset (5,94 and 5,14 respectively).

Figure 4. Distribution pyramid histograms of the Z-score values for the satellite-based dataset (left) and ground-based dataset (right).

Scatterplots were created to display the relationship between the two datasets. First, all ground-based measurements over the study period and the satellite-based measurements from corresponding OMI pixels were plotted (Fig. 5 a). Secondly, the average values of each ground-based measurement station were plotted against the average value of corresponding OMI pixels (Fig. 5 b). Thirdly, the annual averages of all ground-based stations and the annual average of all corresponding OMI pixels were plotted against each other (Fig. 5 c). Finally, the monthly averages of all ground-based data were plotted against the monthly average of all corresponding OMI pixels (Fig. 5 d). All components were significantly correlated at the 0.01 significance level. The linear regressions and Pearson's correlation analyses show that OMI data was more successful at estimating the temporal patterns (r^2 = 0.88, r = 0.94) than the spatial patterns (r^2 = 0.41, r = 0.64). The monthly averages were negatively correlated (r^2 = 0.91, r = -0.96). According to the satellite-based data, the NO_2 concentrations were lowest during the winter months and highest during the summer months, while the pattern for the ground-based data was the opposite. Because of this, it was decided not to use the monthly averages for further analysis in this study.
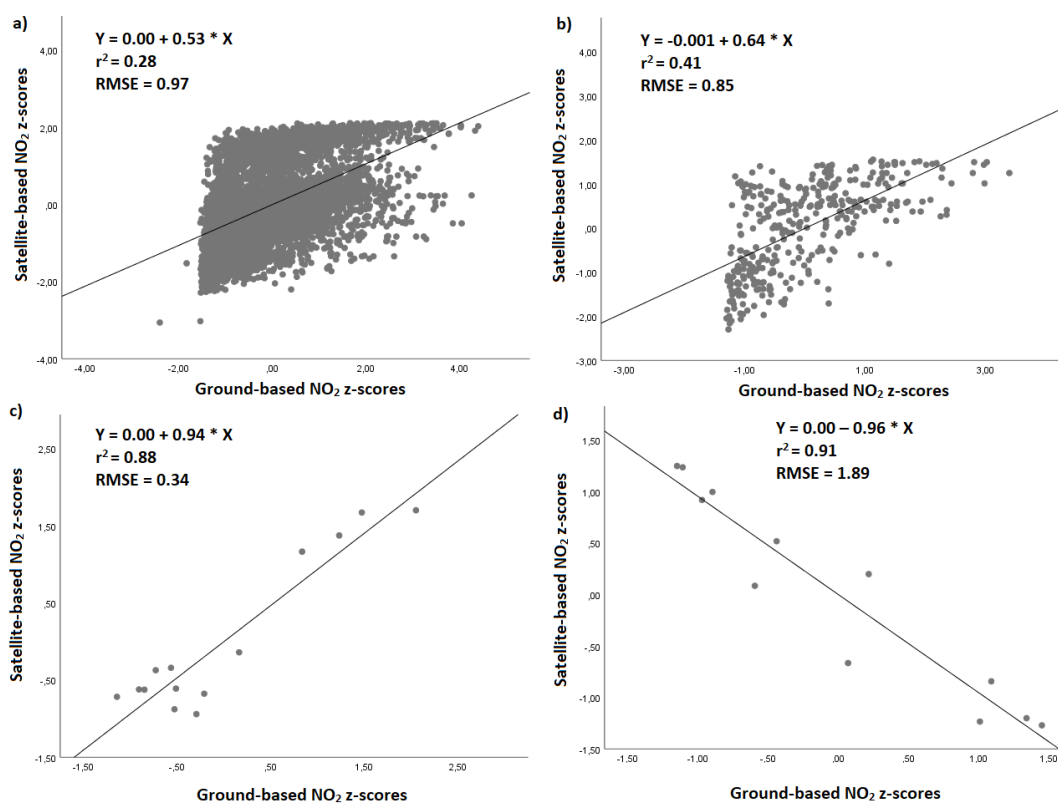
Figure 5. Linear regression and RMSE of the z-scores from (a) the measurements of all ground-based stations against the estimates of corresponding satellite-based pixels, (b) the average value of each ground-based station versus the average value of corresponding satellite-based pixels, (c) the annual averages of all ground-based stations versus the annual averages of corresponding satellite-based pixels, and the monthly averages of all ground-based stations versus the monthly averages of corresponding satellite-based pixels (d).

5.2. Spatial patterns

There is a distinct difference in the concentration distribution between the northern and southern hemispheres, where the higher concentrations are almost exclusively found in the northern hemisphere (Fig. 6 a). The primary hotspot areas that stand out are: 1) U.S.A (Fig. 6 b), 2) western Europe (Fig. 6 c), and 3) India, China and Japan (Fig. 6 d). These areas were selected as focus areas due to their high average NO_2 concentrations and have been used for further analysis in the remaining part of the study.

The range of NO_2 concentrations (Fig. 7), i.e. the variability of concentrations, generally follows the same spatial pattern as the averaged concentrations (Fig. 6). Large areas over the US (Fig. 7 a), Europe (Fig. 7 b), India, eastern China and Japan (Fig. 7 c) have high range values, indicating high variability in NO_2 concentrations over the study period over these areas.

16
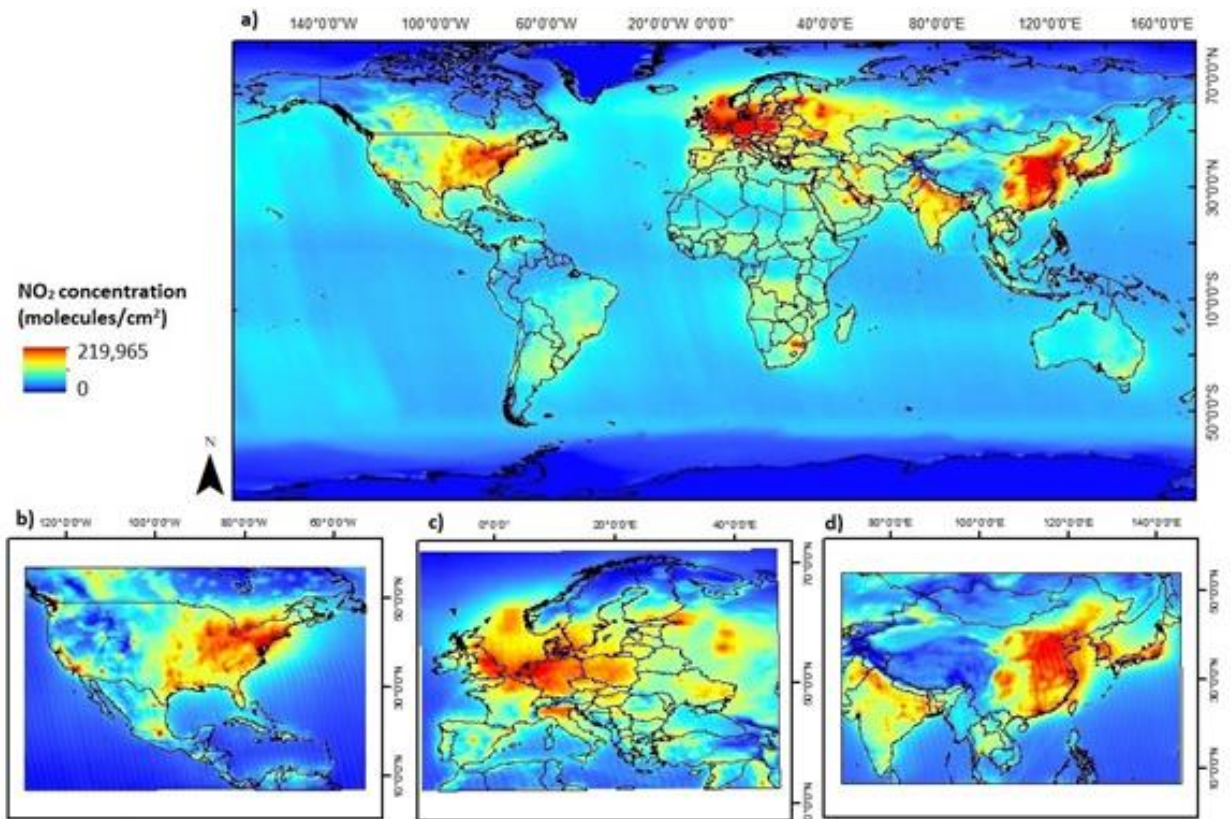
Figure 6. Averaged spatial distribution of tropospheric NO$_2$ concentrations (molecules cm^{-2}) globally (a) and regionally (USA (b), Europe (c), India, China, Japan (d)) between 2005 - 2018.
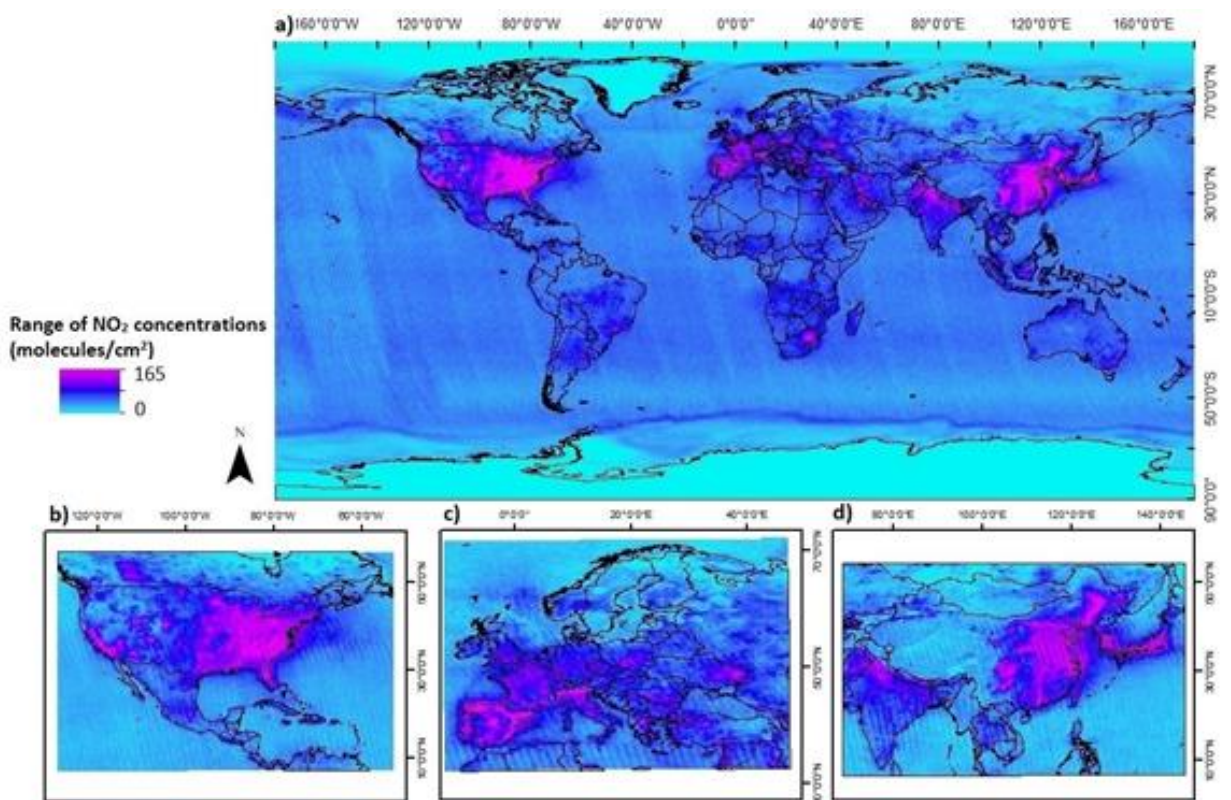
Figure 7. Range of tropospheric NO$_2$ concentrations (molecules cm^{-2}) for each cell globally (a) and regionally (USA (b), Europe (c), India, China, Japan (d)) between 2005 - 2018.

5.3. Temporal trends

The global annual averages of tropospheric NO_2 concentrations shows a decreasing trend over the study period (Fig. 8). After the year 2008, there was a distinct drop which lasted until 2011, when the average concentration was at its lowest point of the study period (37.11 molecules cm^{-2}). After 2011, the concentrations started to increase again. Even though the time series has a negative linear trend, the annual average of the year 2018 is the highest over the study period (52.05 molecules cm^{-2}).
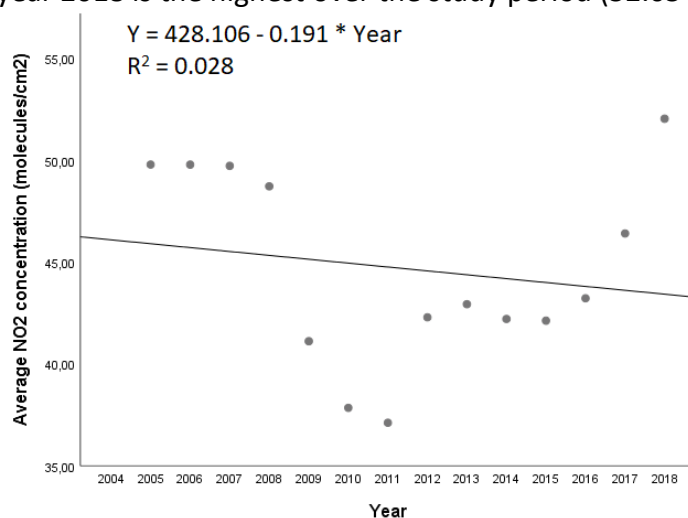
Figure 8. Time series of global annual average tropospheric NO_2 concentrations (molecules cm^{-2}) 2005-2018.

Just over half of the study area (53 %) had decreasing trends over the study period, while 47 % had positive (Fig. 9). An interesting pattern that stands out is the relationship between increasing trends over oceans and decreasing trends over land. Out of all cells over oceans, 79.98 % had positive trends, and out of all cells over land, 70.89 % had decreasing trends. The increasing trends were generally found near the poles, west of the Americas, as well as along vertical strips in the southern hemisphere.

With the insignificant trends (significance level 0.05) masked out, 72.12 % of the remaining cells were negative whereas 27.88 % were positive (Fig. 10 a). 91.08 % of the negative significant trends were located over land and 65.99 % of the positive significant trends were located over oceans. Hereafter, all trends described in this paper refer to significant trends. The average significant trend globally over the study period was -0.41 molecules $cm^{-2}\,y^{-1}$. The average significant trend over land was -1.84 molecules $cm^{-2}\,y^{-1}$ while the average significant trend over oceans was 0.35 molecules $cm^{-2}\,y^{-1}$.
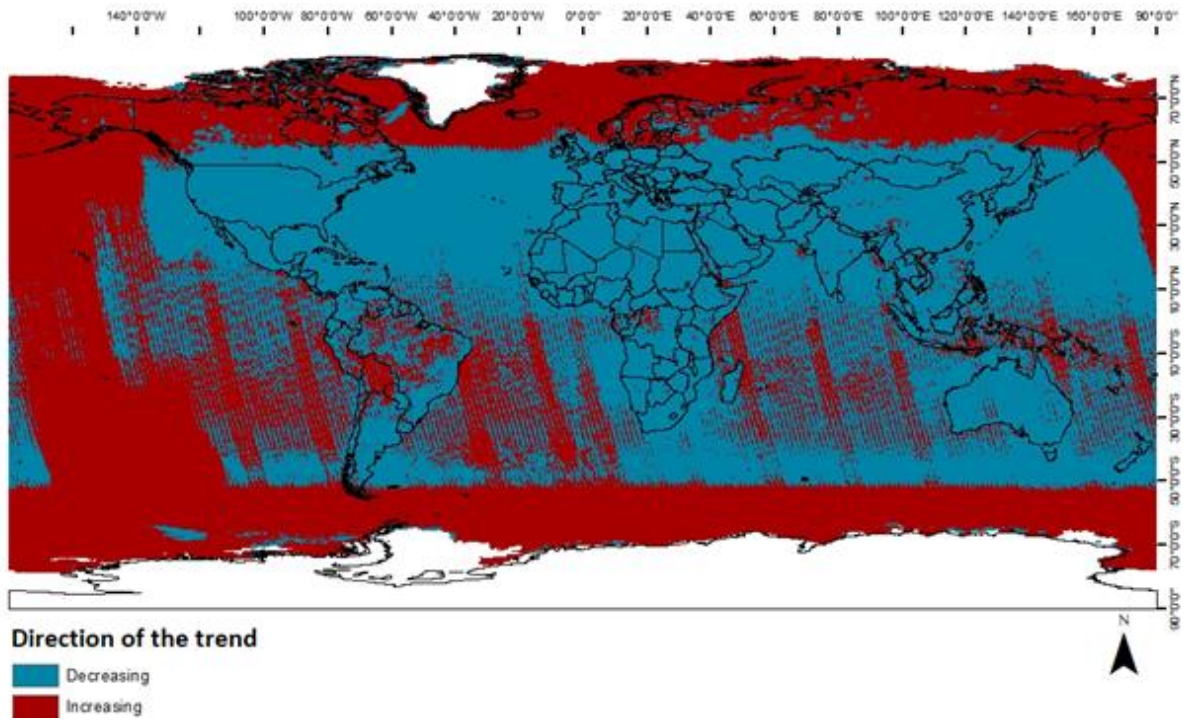
Figure 9. Direction of each cell's trend globally between 2005 – 2018 as estimated by Polytrend.
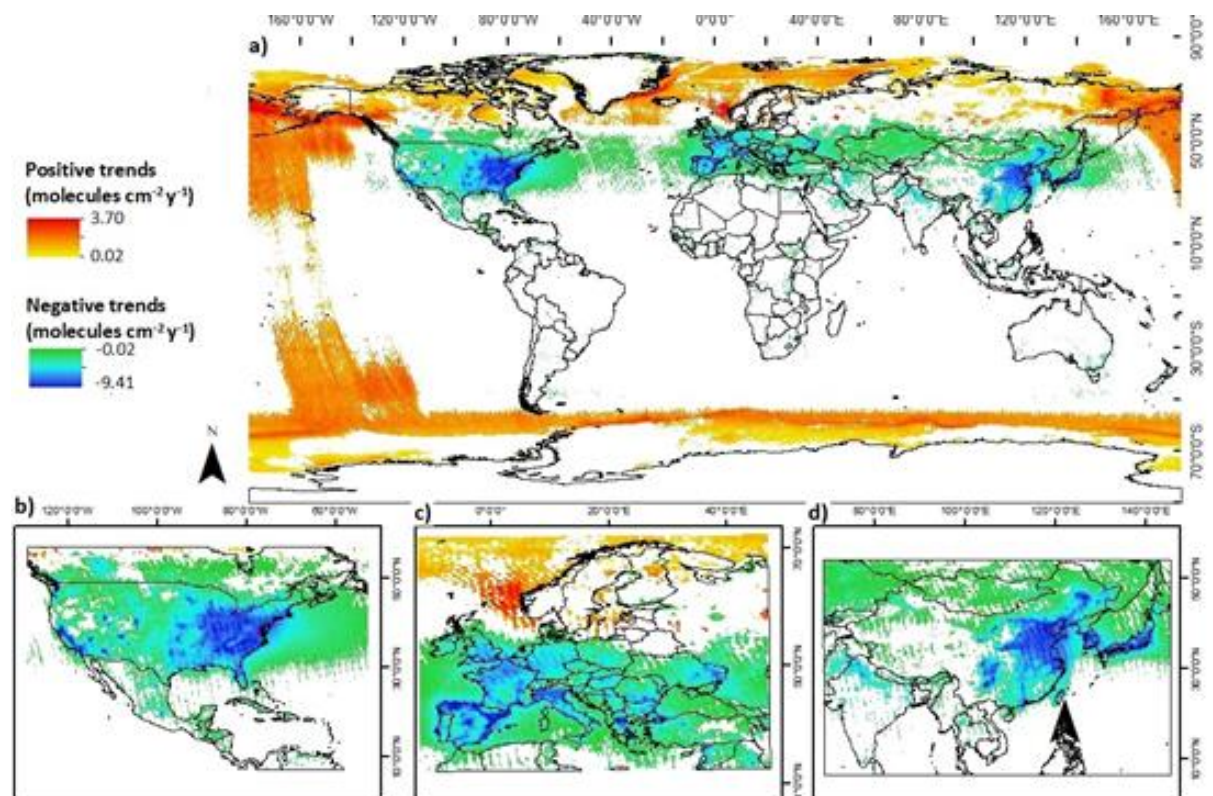
Figure 10. Direction of each significant cell's trend and coefficients as estimated by Polytrend globally (a) and regionally (USA (b), Europe (c), India, China, Japan (d)) between 2005 - 2018.

All areas with high average NO_2 concentrations (Fig. 6) and high variability (Fig. 7) also had negative significant trends (Table 1). The strongest average trends in the focus areas were found in Japan (- 5.11 molecules $cm^{-2} y^{-1}$), Belgium (- 4.89 molecules $cm^{-2} y^{-1}$) and Germany (- 4.04 molecules $cm^{-2} y^{-1}$). The highest average NO_2 concentrations were found in the Netherlands (206.18 molecules cm^{-2}), Belgium (191.17 molecules cm^{-2}), Germany (184.67 molecules cm^{-2}) and the U.K. (160.48 molecules cm^{-2}). All of these countries are located in Europe, where the highest maximum concentrations were also found.

Table 1 The major, average and range of change (molecules cm-2) of significant breakpoints during the year 2008, as well as the proportion of the type of change.

Country	Average NO_2 concentration	Max NO_2 concentration	Average range	Max range	Average trend	Strongest trend	
						+	-
USA	91.80	192.76	54.51	141	- 3.57	2.60	- 9.38
Netherlands	206.18	214.12	50.68	65	- 3.79	-	- 5.38
Belgium	191.17	211.49	62.43	77	- 4.89	-	- 6.32
Germany	184.67	216.57	57.77	81	- 4.04	-	- 6.20
U.K.	160.48	214.85	50.46	87	- 3.79	1.15	- 6.91
India	116.42	188.32	54.26	135	- 3.11	3.49	- 6.56
China	98.48	195.75	48.94	129	- 3.57	2.17	- 8.29
Japan	139.32	190.51	76.57	114	- 5.11	-	- 8.26
Global	44.67	219.97	22.18	165	- 0.41	3.70	- 9.41

5.4. Trend types

In a global context, the quadratic trend type had the highest spatial coverage (44.42 %, mainly positive) (Table 2) out of which 44.80 % is found over land and 55.20 % is found over oceans. The cubic trend type occupies 32.59 % of the significant trends, out of which 95.10 % is found over oceans. 22.99 % had a linear trend type, mainly negative, out of which 57.34 % is found over land and 42.66 % is found over oceans (Fig. 11 a). The proportional coverage of the trend types in the focus areas can be seen in figure 11 b – d and are summarised in table 2.
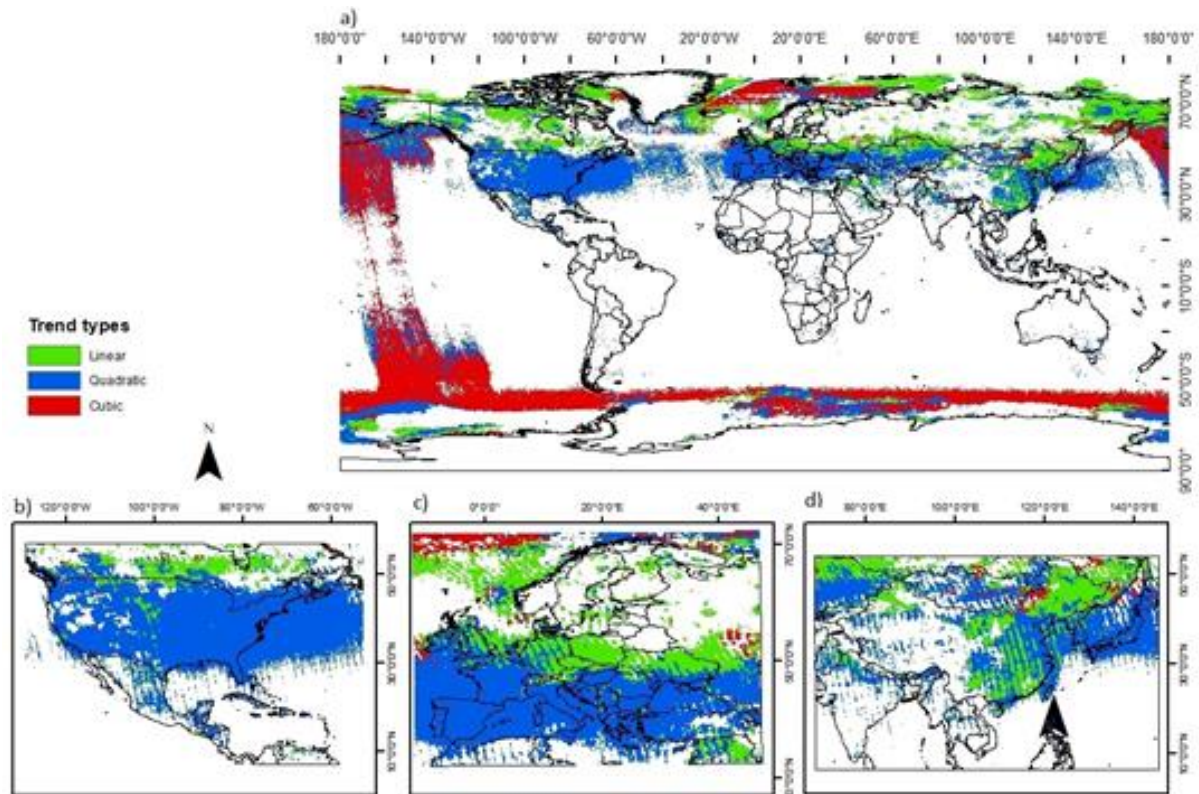
Figure 11. Trend type of each cell with a significant trend globally (a) and in USA (b), Europe (c), India, China, Japan (d) between 2005 – 2018 as estimated by Polytrend.

Table 2. Spatial coverage (%) of the significant trend types globally and in average NO2 concentration hotspot areas.

	Trend types						
	Linear	Linear	Quadratic	Quadratic	Cubic	Cubic	Cell count
Trend Direction	+	-	+	-	+	-	
USA	0.00	4.52	6.48	87.65	1.18	0.17	14 074
Netherlands	0.00	60.56	0.00	39.44	0.00	0.00	71
Belgium	0.00	25.81	0.00	74.19	0.00	0.00	62
Germany	0.00	60.87	0.00	39.13	0.00	0.00	736
U.K.	0.44	41.67	0.00	57.89	0.00	0.00	456
India	0.38	14.08	0.09	85.07	0.19	0.19	1 065
China	0.03	47.12	0.02	49.49	0.01	3.32	8 883
Japan	0.00	2.16	0.00	97.84	0.00	0.00	602
Global	5.07	17.92	33.59	10.83	7.62	24.97	87 889

5.5. Breakpoint analysis

The starting time of the detected breakpoints (insignificant changes masked out) is dominated by the period of 2005 – 2008 (71.97 % of cells) (Fig. 12 a). The year 2008 was by far the year with the highest occurrence of major changes of all years (46.31 %), indicating a major event during this year that had effects all over the globe (Fig. 12 a and Fig. 13).

The detected breakpoints were mostly negative (63.67 %) (Fig. 12 b) and non-abrupt (85.17 %), indicating that most of the changes occurred gradually over time. The cells that experienced the strongest positive change over the study period are located in South Africa (61.37 molecules cm^{-2}), China (57.81 molecules cm^{-2}) and India (56.90 molecules cm^{-2}) while the cells that experienced the strongest negative change are located in China (97.92 molecules cm^{-2}), USA (-91.12 molecules cm^{-2}) and Spain (-83.02 molecules cm^{-2}). Because of the drastic changes in 2008, this year was investigated further (Fig. 13). 98.74 % of the major changes were negative (Fig. 13 a) out of which 71.70 % were non-abrupt. In the focus areas, the strongest change of 2008 was in China (-97.92 molecules cm^{-2}) where most of the changes were non-abrupt, followed by USA (-91.12 molecules cm^{-2}). The strongest average change was in Japan (-44.62 molecules cm^{-2}), followed by USA (-41.47 molecules cm^{-2}).
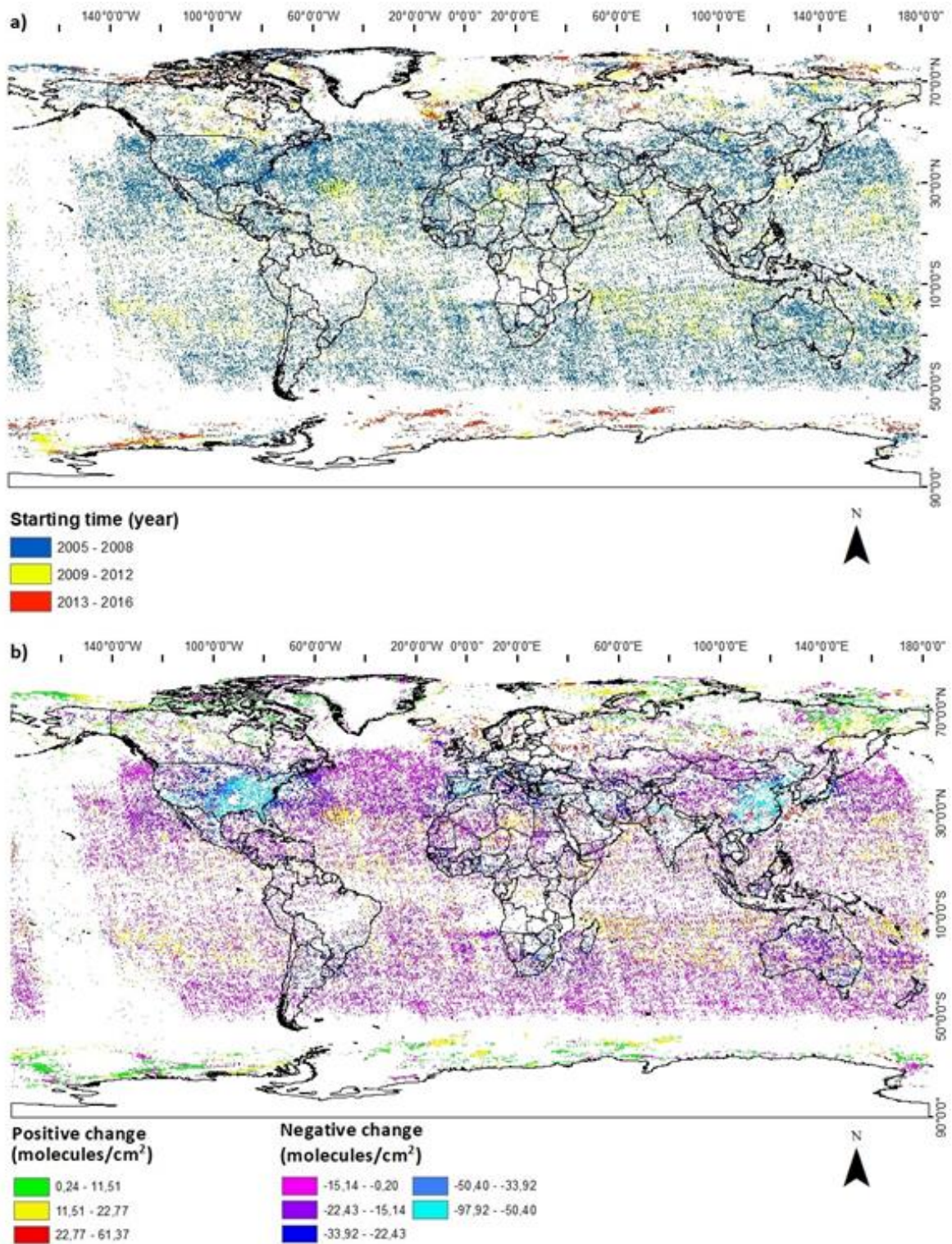
Figure 12. The starting year (a) and magnitude (b) of the major change for each significant cell between 2005 – 2018, as estimated by DBEST.
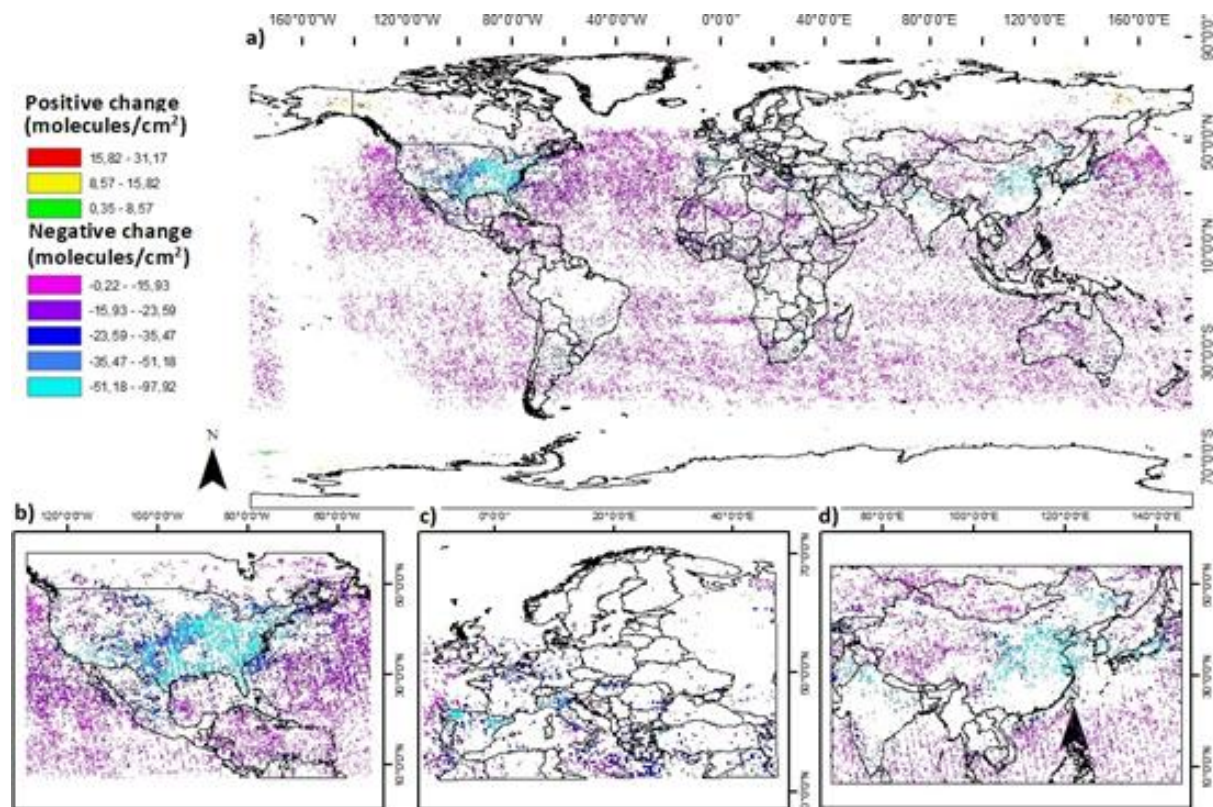
Figure 13. The major change of each significant cell globally (a) and in USA (b), Europe (c), India, China, Japan (d) during the year 2008, as estimated by DBEST.

Table 3 The major, average and range of change (molecules cm-2) of significant breakpoints during the year 2008, as well as the proportion of the type of change.

	Major change	Average change	Range of change values	Change type (%)	
				Abrupt	Non-abrupt
USA	-91.12	-41.47	122.29	85.08	14.92
Netherlands	-28.93	-22.98	13.92	58.33	41.67
Belgium	-33.15	-27.47	15.39	14.29	85.71
Germany	-50.55	-31.86	38.77	62.92	37.08
U.K.	-37.63	-24.44	22.57	41.30	58.70
India	-60.56	-34.61	47.23	23.36	76.64
China	-97.92	-32.45	90.96	42.20	57.80
Japan	-76.81	-44.62	60.75	38.82	61.18
Global	-97.92	-18.62	129.09	28.30	71.70

6. Discussion

This study contributes to the ongoing research regarding remote sensing of spatiotemporal NO_2 trends by validating the OMI NO_2 product and by investigating how the tropospheric concentrations have changed globally and regionally over the period of 2005 through 2018. Furthermore, the timing and magnitude of the major change for each cell with a significant trend was highlighted. The most important results of the study show that the regions that have the highest average concentrations also have the highest variability and negative trends, that the global trend in NO_2 over the study period is negative, and that in year 2008 something happened that had a significant and sudden impact on the global concentrations of NO_2.

6.1. OMI validation

The results of the OMI validation showed that there was statistically significant agreement between the satellite-based and the ground-based datasets. The correlations were statistically significant at the 0.01 level for all components and the correlation coefficient for all of the data points was 0.53 (Fig. 5 a). This result is in line with previous OMI validation studies. For instance, the correlation coefficients ranged between $0.47 - 0.76$ in a study of several cities by de Foy et al. (2016), $0.51 - 0.86$ by Paraschiv et al. (2017), $0.4 - 0.8$ by Bechle et al. (2013) and 0.76 for Lamsal et al. (2015). The statistical comparison further indicated that OMI was more successful at estimating the temporal component (r = 0.93) than the spatial component (r = 0.64). This can partially be explained by that the ground-based monitoring stations is focused on a certain emission source, e.g. traffic locations, whereas an OMI pixel (13 * 24 km^2) covers a larger area with more potential emission sources within the pixel (Paraschiv et al., 2017). Based on this, it is concluded that satellite-based measurements from OMI is a useful approach for measurements of NO_2 in order to compensate for the lacking spatial coverage of ground-based monitoring stations and to study global trends.

6.2. Spatiotemporal trends

The spatial distribution of average NO_2 concentrations found in this study (Fig. 6) resemble those in similar studies (Georgoulias et al. 2019; Krotkov et al. 2016; Miyazaki et al., 2017; Geddes et al., 2015), confirming that these areas are indeed the main hotspots of tropospheric NO_2 concentrations globally. According to Krotkov et al. (2016), the highest NO_2 concentrations coincide with urban areas with high populations and industrialized regions. The global and regional NO_2 temporal trends found in this study (Fig. 10) also generally agree with the results from previous studies, with two differences. Georgoulias et al. (2019), Miyazaki et al. (2017) and Geddes et al. (2015) all reported increasing NO_2 trends over both India and China, while Krotkov et al. (2016) reported increasing trends over India. In this study, the results show decreasing trends over both countries. Reasons for this difference can possibly be attributed to differences in satellite instruments used and/or study periods. Geddes et al. (2015) combined data from GOME, GOME-2 and SCIAMACHY from 1996 through 2012, Miyazaki et al. (2017) combined data from OMI, GOME-2 and SCIAMACHY

between 2005 and 2014, Georgoulias combined GOME, GOME-2 and SCIAMACHY between 1996 and 2017, and Kroktov et al (2016) used OMI data from 2005 through 2015.

The global average of the significant trends over the study period was negative (- 0.41 cm^{-2} y^{-1}), but differences over land and oceans were observed. Over land, the average trend was -1.84 cm^{-2} y^{-1}, while the average trend over ocean areas was 0.35 cm^{-2} y^{-1}. It should be noted that all though the global average trend and the average trend over land were negative over the full study period, the global annual averages actually increased over the second half of the study period (Fig. 8). It is plausible that the negative trends are biased by the temporary dip in concentrations during the years 2008 – 2011.

NO_2 concentrations over oceans are generally much lower than over terrestrial areas since there are no sources of NO_2 emissions except for passing ships (Peters et al., 2012), which indicates that the increasing trends over remote oceans are caused by atmospheric deposition of NO_2 which has been transported from their source by large-scale circulation (Yuchechen et al., 2017). According to Peters et al. (2012), satellite instruments have issues detecting trace gases over remote oceans because concentrations are very low, and the concentrations are often below the detection limit of the instruments.

Decreases of NO_2 concentrations can primarily be attributed to either local, regional or country level environmental regulations, improvements in emission control technology (for e.g. power plants and vehicles), or economic changes and the associated effects in energy usage (Duncan et al., 2016; Krotkov et al., 2016). Since the spatial distribution of average concentrations and decreasing significant trends correlate well, this indicates that environmental regulations and technological improvements in the countries with the most severe pollution have had a positive effect on concentrations of NO_2. However, it should also be noted that the final year of this study period (2018) has the highest average global concentrations of all years in this study. It is plausible that economic changes also had an effect, based on the sudden decrease after the year 2008, which was the starting year of a global economic recession (Bishop & Steadman, 2014; Castellanos & Boersma, 2012) (cf below). This clearly shows the importance of satellite-based monitoring of NO_2 concentrations for assessing global trends, the effects of regional environmental regulations and technological improvements to reduce emissions, but also for estimations of marine background conditions for global and regional chemical transport models (Martins et al., 2016).

6.3. Linear and non-linear trend types

Linear regression models assume that changes occur linearly and gradually, which is not always the case (Jamali et al., 2014). Here, a polynomial fitting-based scheme (Polytrend) was used to account for non-linear trends. This polynomial approach thus helps to detect remotely sensed trends in a time series that would not be identified by an ordinary least square (i.e. linear model) approach. The linear trend type was the least common trend globally, while the quadratic trend type was the most common trend (Fig. 11; Table 2). Since the quadratic trend type has a trend line with one bend, this indicates that these areas either increased in the beginning of the study period and then started to decrease, or that they have been decreasing over the study period and started to increase towards the end of the study period. The cubic trend type was uncommon in all NO_2 hotspot countries and was almost exclusively found over oceans (95.10 %). This means that the trend direction over these cells changed multiple times and could be an indication of the statement from Peters et al. (2012) that measurements over remote oceans are unclear. Based on this, it should be noted that the positive trends over remote ocean areas are possibly unreliable, due to that the concentrations in these areas are low in relation to the magnitude of the error sources.

6.4. Breakpoint analysis

The majority of the significant breakpoints over the study period were negative (63.67 %) and non-abrupt (85.17 %). Non-abrupt changes indicate that the concentrations of NO_2 have increased or decreased gradually, possibly due to environmental regulations that have become stricter over time or economic cycles, as opposed to abrupt changes which could be due to that power plants or industries have been either opened or shut down suddenly.

The year 2008 was by far the year with the highest occurrence of significant breakpoints (46.31 %), out of which 98.74 % was negative. A global-scale reduction of tropospheric NO_2 concentrations was also observed in figure 8 during this year. It has also previously been pointed out that 2008 is a year of significant reductions in NO_2 emissions (e.g. Tong et al., 2015; de Foy et al., 2016; Bishop & Steadman, 2014; Castellanos & Boersma, 2012) due to the start of the so called 'Great Recession'. This was an event which caused large scale economic reductions and affected anthropogenic activity globally, which in turn reduced the associated emissions of air pollution from e.g. vehicles, power plants and industries. The plausible impact of the Great Recession on the regional NO_2 hotspots can be seen in figures 13 b, c and d as well as in table 3. According to the results of this study, the largest change magnitudes in NO_2 concentrations during 2008 were found in China, USA, India and Japan. The European countries appear to have suffered less, based on the changes in tropospheric NO_2 concentrations (Fig, 13; Table 3).

Page intentionally left blank.

7. Conclusions

In this study, the spatial patterns and temporal trends of tropospheric NO_2 have been studied globally over the study period of 2005 - 2018 by using remotely sensed satellite data from the OMI instrument aboard NASA's Aura satellite. Furthermore, the timing and magnitude of significant breakpoints were identified.

The OMI data was validated using data from ground-based monitoring stations and there was statistically significant agreement between the satellite-based and the ground-based datasets. This shows that satellite-based measurements are useful for studying trends in tropospheric air pollution and can compensate the lacking spatial coverage of ground-based monitoring stations.

The spatial distribution of NO_2 concentrations is dominated by industrialised and highly populated regions in the northern hemisphere, and eastern USA, western Europe, India, China and Japan were identified as NO_2 concentration hotspots.

The average global trend was negative over the study period (- 0.41 molecules cm^{-2} y^{-1}) and a large difference between ocean and land areas was observed. The average trend over oceans was 0.35 molecules cm^{-2} y^{-1}, while the average trend over land was – 1.84 molecules cm^{-2} y^{-1}. All countries that were identified as NO_2 concentration hotspots had negative average trends.

The timing of the strongest significant breakpoints mostly occurred during the year 2008 (46.31 %), and almost all these breakpoints were negative.

Page intentionally left blank.

8. References

Bishop, G. A. and Stedman, D. H. (2014) 'The recession of 2008 and its impact on light-duty vehicle emissions in three western United States cities', Environmental Science & Technology, 48(24), pp. 14822–14827. doi: 10.1021/es5043518.

Boersma, K. F. *et al.* (2011) 'An improved tropospheric NO2 column retrieval algorithm for the Ozone Monitoring Instrument', *Atmospheric Measurement Techniques Discussions*, 4(2), pp. 2329–2388. doi: 10.5194/amtd-4-2329-2011.

Bucsela *et al.* (2013) 'A new stratospheric and tropospheric NO2 retrieval algorithm for nadir-viewing satellite instruments: applications to OMI', *Atmospheric Measurement Techniques*, (10), p. 2607. doi: 10.5194/amt-6-2607-2013.

Bucsela, E. J. *et al.* (2006) 'Algorithm for NO2 Vertical Column Retrieval From the Ozone Monitoring Instrument', *IEEE Transactions on Geoscience & Remote Sensing*, 44(5), pp. 1245–1258. doi: 10.1109/TGRS.2005.863715.

Castellanos, P. and Boersma, K. F. (2012) 'Reductions in nitrogen oxides over Europe driven by environmental policy and economic recession', Scientific Reports, 2, p. 265. doi: 10.1038/srep00265.

de Foy, B., Lu, Z. and Streets, D. G. (2016) 'Impacts of control strategies, the Great Recession and weekday variations on NO2 columns above North American cities', Atmospheric Environment, 138, pp. 74–86. doi: 10.1016/j.atmosenv.2016.04.038.

Dobber et *al*. (2006) 'Ozone monitoring instrument calibration', *IEEE Transactions on Geoscience and Remote Sensing, Geoscience and Remote Sensing, IEEE Transactions on, IEEE Trans. Geosci. Remote Sensing*, (5), p. 1209. doi: 10.1109/TGRS.2006.869987.

Earthdata (2019) 'OMI/Aura NO2 Cloud-Screened Total and Tropospheric Column L3 Global Gridded 0.25 degree x 0.25 degree V3 (OMNO2d) at GES DISC' NASA. Available at: https://search.earthdata.nasa.gov/search/granules?p=C1266136111-GES_DISC&m=-28.40625!199.96875!0!1!0!0%2C2&tl=1541162947!4!!&q=no2&ok=no2

GADM (2018) https://gadm.org/download_world.html

Geddes, J. A. *et al.* (2016) 'Long-Term Trends Worldwide in Ambient NO2 Concentrations Inferred from Satellite Observations', *Environmental Health Perspectives*, 124(3), pp. 281–289. doi: 10.1289/ehp.1409567.

Georgoulias, A. K. *et al. (2019) 'Trends and trend reversal detection in 2 decades of tropospheric NO2 satellite observations',* Atmospheric Chemistry & Physics, 19(9), p. 6269. Available at: http://search.ebscohost.com.ludwig.lub.lu.se/login.aspx?direct=true&db=edb &AN=136542711&site=eds-live&scope=site (Accessed: 28 May 2019).

Gilliam, J. & Hall, E. (2016) 'Reference and Equivalent Methods Used to Measure National Ambient Air Quality Standards (NAAQS) Criteria Air Pollutants - Volume I'. U.S. Environmental Protection Agency, Washington, DC, EPA/600/R-16/139, 2016.

Goldberg *et al.* (2019) 'A top-down assessment using OMI NO2 suggests an underestimate in the NOx emissions inventory in Seoul, South Korea, during KORUS-AQ', *Atmospheric Chemistry and Physics*, p. 1801. doi: 10.5194/acp-19-1801-2019.

Hains, J. C. *et al.* (2010) 'Testing and improving OMI DOMINO tropospheric NO2 using observations from the DANDELIONS and INTEX-B validation campaigns', *Journal of Geophysical Research. Atmospheres*, 115(D5), p. n/a. Available at: http://search.ebscohost.com/login.aspx?direct=true&db=edb&AN=87219477& site=eds-live&scope=site (Accessed: 9 May 2019).

Ialongo *et al.* (2016) 'Comparison of OMI NO2 observations and their seasonal and weekly cycles with ground-based measurements in Helsinki', *Atmospheric Measurement Techniques*, (10), p. 5203. doi: 10.5194/amt-9-5203-2016.

Jamali, S. *et al.* (2015) 'Detecting changes in vegetation trends using time series segmentation', *Remote Sensing of Environment*, (January), p. 182. doi: 10.1016/j.rse.2014.09.010.

Jamali, S. *et al.* (2014) 'Automated mapping of vegetation trends with polynomials using NDVI imagery over the Sahel', *Remote Sensing of Environment*, 141, pp. 79–89. doi: 10.1016/j.rse.2013.10.019.

Kim, H. C. *et al.* (2018) 'A conservative downscaling of satellite-detected chemical compositions: NO2 column densities of OMI, GOME-2, and CMAQ', *Remote Sensing*, 10(7). doi: 10.3390/rs10071001.

Krotkov *et al*. (2017) 'The version 3 OMI NO2 standard product', Atmospheric Measurement Techniques, p. 3133. doi: 10.5194/amt-10-3133-2017.

Lamsal, L. N. *et al.* (2015) 'U.S. NO2 trends (2005–2013): EPA Air Quality System (AQS) data versus improved observations from the Ozone Monitoring Instrument (OMI)', *Atmospheric Environment*, 110, pp. 130–143. doi: 10.1016/j.atmosenv.2015.03.055.

Levelt, P. F., & Noordhoek, R. (2002). OMI Algorithm Theoretical Basis Document Volume I: OMI Instrument, Level 0-1b Processor, Calibration & Operations [Online]. Technology Report ATBD-OMI-01, Version, 1. Available from: http://projects.knmi.nl/omi/documents/data/OMI_ATBD_Volume_1_V1d1.pdf Last updated 16-Dec-2008 [25 April 2019]

Levelt, P. *et al.* (2017) 'The Ozone Monitoring Instrument: Overview of twelve years in space', *Atmospheric Chemistry & Physics Discussions*, p. 1. Available at: http://search.ebscohost.com.ludwig.lub.lu.se/login.aspx?direct=true&db=edb &AN=124413602&site=eds-live&scope=site (Accessed: 26 April 2019).

Martins, D. K. et al. (2016) 'Spatial and temporal variability of ground and satellite column measurements of NO2 and O3 over the Atlantic Ocean during the Deposition of Atmospheric Nitrogen to Coastal Ecosystems Experiment', Journal of Geophysical Research. Atmospheres, 121(23), p. 14,175. Available at: http://search.ebscohost.com.ludwig.lub.lu.se/login.aspx?direct=true&db=edb &AN=120505229&site=eds-live&scope=site (Accessed: 28 May 2019).

McPeters *et al.* (2008), *Validation of the Aura Ozone Monitoring Instrument total column ozone product, J. Geophys. Res., 113, D15S14, doi:10.1029/2007JD008802.*
Munir, S. *et al.* (2013) 'Quantifying temporal trends of atmospheric pollutants in Makkah (1997–2012)', *Atmospheric Environment*, 77, pp. 647–655. doi: 10.1016/j.atmosenv.2013.05.075.

NASA (2007) 'NASA's Aura: New Eye for Clean Air' [Online]. Available from: https://www.nasa.gov/vision/earth/lookingatearth/aura_first.html Last modified 30-Nov-2007.

OMI Team (2012) 'Ozone Monitoring Instrument (OMI) data user's guide' [Online]. OMI-DUG-5.0, NASA. Washington DC: NASA. 62 pp. Available from: https://acdisc.gesdisc.eosdis.nasa.gov/data/Aura_OMI_Level3/OMAEROe.003/ doc/README.OMI_DUG.pdf Last modified 22-Feb-2019 [25 April 2019]

Palmer, P. I. *et al.* (2001) 'Air mass factor formulation for spectroscopic measurements from satellites: Application to formaldehyde retrievals from the Global Ozone Monitoring Experiment', *Journal of Geophysical Research. Atmospheres*, 106(D13), p. 14539. Available at: http://search.ebscohost.com.ludwig.lub.lu.se/login.aspx?direct=true&db=edb &AN=87211814&site=eds-live&scope=site (Accessed: 17 May 2019).

Peters et al. (2012) 'Formaldehyde and nitrogen dioxide over the remote western Pacific Ocean: SCIAMACHY and GOME-2 validation using ship-based MAX-DOAS observations', Atmospheric Chemistry and Physics, (22), p. 11179. doi: 10.5194/acp-12-11179-2012.

Safieddine, S. et al. (2013) 'Tropospheric ozone and nitrogen dioxide measurements in urban and rural regions as seen by IASI and GOME-2', Journal of Geophysical Research. Atmospheres, 118(18), p. 10,555. Available at: http://ludwig.lub.lu.se/login?url=http://search.ebscohost.com.ludwig.lub.lu.se/login.aspx?direct=true&db=edb&AN=91102726&site=eds-live&scope=site (Accessed: 14 January 2019).

Schneider, W. A. Lahoz and R. van der A (2015) 'Recent satellite-based trends of tropospheric nitrogen dioxide over large urban agglomerations worldwide', *Atmospheric Chemistry and Physics*, (3), p. 1205. doi: 10.5194/acp-15-1205-2015.

Tan, W. *et al.* (2018) 'Tropospheric NO2, SO2, and HCHO over the East China Sea, using ship-based MAX-DOAS observations and comparison with OMI and OMPS satellite data', *ATMOSPHERIC CHEMISTRY AND PHYSICS*, 18(20), pp. 15387–15402. doi: 10.5194/acp-18-15387-2018.

Tong, D. Q. et al. (2015) 'Long-term NOx trends over large cities in the United States during the great recession: Comparison of satellite retrievals, ground observations, and emission inventories', Atmospheric Environment, 107, pp. 70–84. doi: 10.1016/j.atmosenv.2015.01.035.

Torres, O. (1) *et al.* (2018) 'Impact of the ozone monitoring instrument row anomaly on the long-term record of aerosol products', *Atmospheric Measurement Techniques*, 11(5), pp. 2701–2715. doi: 10.5194/amt-11-2701-2018.

US EPA (2002) 'Quality Assurance Guidance Document 2.3 – Reference Method for the Determination of Nitrogen Dioxide in the Atmosphere (Chemiluminescence)'. U.S. Environmental Protection Agency [online] Available at https://www3.epa.gov/ttn/amtic/files/ambient/pm25/qa/no2.pdf

US EPA (2019) https://aqs.epa.gov/aqsweb/airdata/download_files.html#Annual

WHO (2016) 'Ambient air pollution: a global assessment of exposure and burden of disease' [Online]. World Health Organization, Geneva. available from http://www.who.int/iris/handle/10665/250141 (Accessed: 3 May 2019).

Xie, Y., Wang, W. and Wang, Q. (2018) 'Spatial Distribution and Temporal Trend of Tropospheric NO2 over the Wanjiang City Belt of China', *Advances in Meteorology*, pp. 1–13. doi: 10.1155/2018/6597186.

Yu, T. *et al.* (2018) 'An assessment of air-quality monitoring station locations based on satellite observations', *International Journal of Remote Sensing*, 39(20), pp. 6463–6478. doi: 10.1080/01431161.2018.1460505.

Yuchechen, A., Gabriela Lakkis, S. and Canziani, P. (2017) 'Linear and Non-Linear Trends for Seasonal NO2 and SO2 Concentrations in the Southern Hemisphere (2004-2016)', Remote Sensing, 9(9), p. 891. doi: 10.3390/rs9090891.

Zhang, L. et al. (2017) 'Spatial and temporal evaluation of long term trend (2005–2014) of OMI retrieved NO2 and SO2 concentrations in Henan Province, China', Atmospheric Environment, 154, pp. 151–166. doi: 10.1016/j.atmosenv.2016.11.067.

Zhang, R. *et al.* (2018) 'Comparing OMI-based and EPA AQS in situ NO2 trends: towards understanding surface NOx emission changes', *Atmospheric Measurement Techniques*, 11(7), pp. 3955–3967. doi: 10.5194/amt-11-3955-2018.

Ziemke *et al.* (2017) 'A cloud-ozone data product from Aura OMI and MLS satellite measurements', *Atmospheric Measurement Techniques*, p. 4067. doi: 10.5194/amt-10-4067-2017.

Page intentionally left blank.

9. Appendices

9.1. Change types

Change type
- Insignificant
- Non-abrupt
- Abrupt
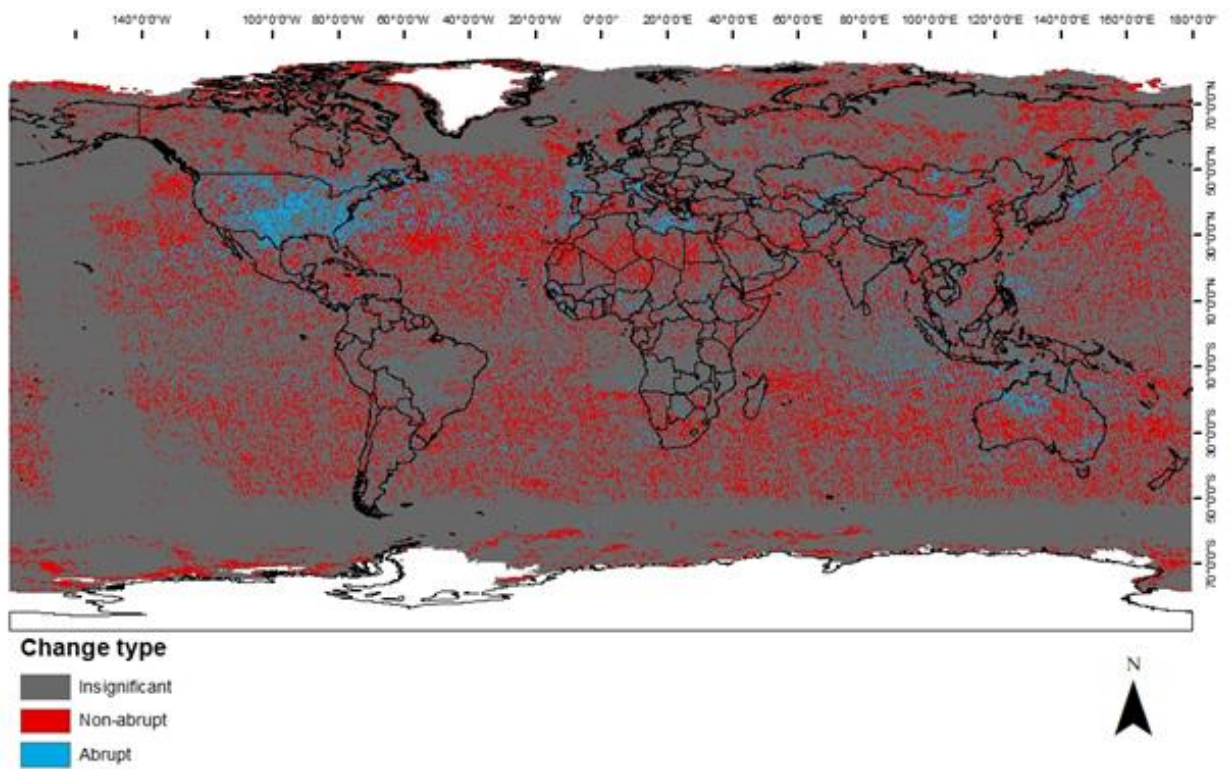
Figure 14. Type of change as estimated by DBEST.

9.2. Significant change

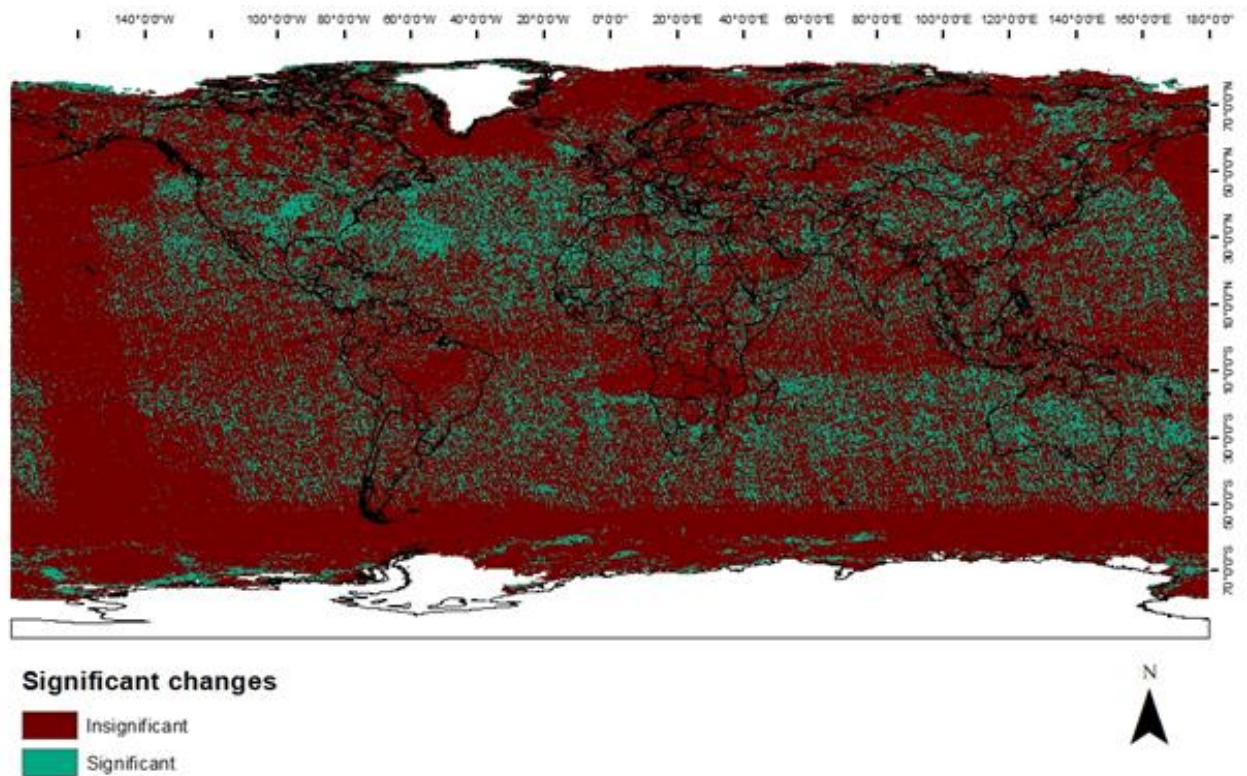Significant changes
- Insignificant
- Significant

Figure 15. Significance of change per cell as estimated by DBEST.
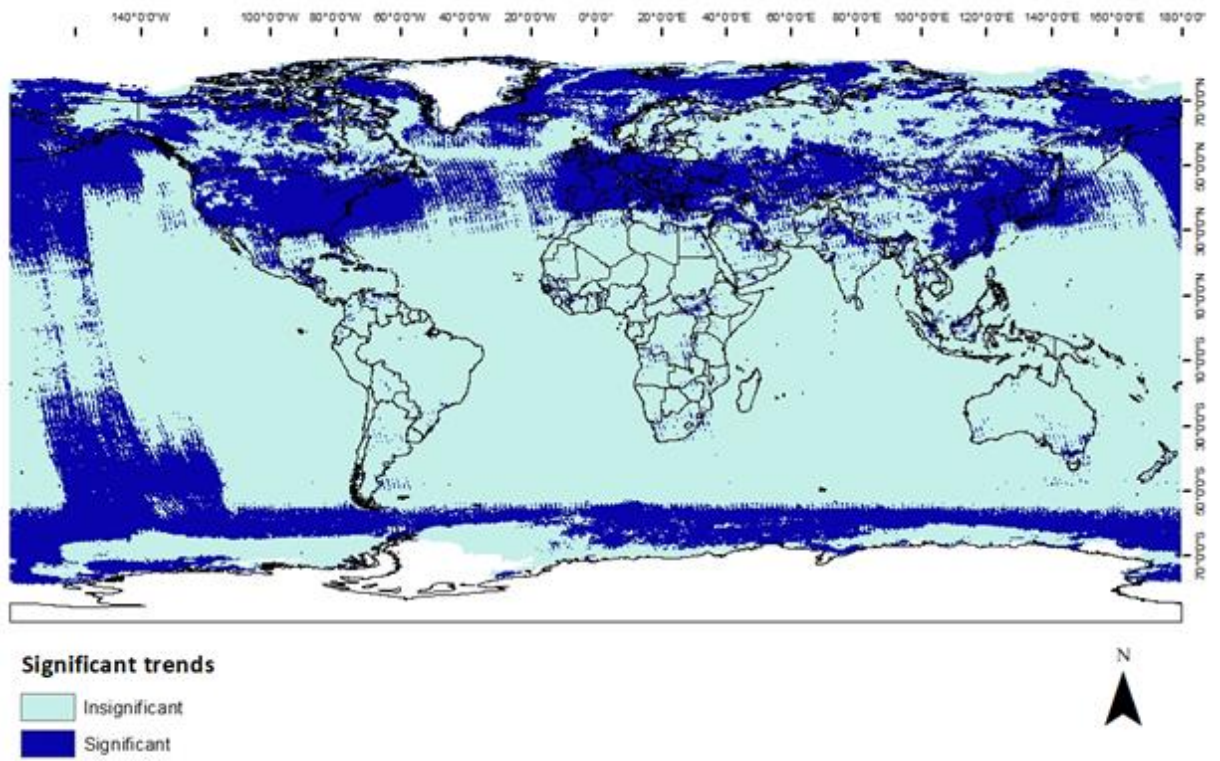
9.3. Significant trends

Figure 16. Significance of trends per cell as estimated by Polytrend.

9.4. List of previously published master thesis reports

Series from Lund University
Department of Physical Geography and Ecosystem Science

Master Thesis in Geographical Information Science

1. *Anthony Lawther:* The application of GIS-based binary logistic regression for slope failure susceptibility mapping in the Western Grampian Mountains, Scotland (2008).
2. *Rickard Hansen:* Daily mobility in Grenoble Metropolitan Region, France. Applied GIS methods in time geographical research (2008).
3. *Emil Bayramov:* Environmental monitoring of bio-restoration activities using GIS and Remote Sensing (2009).
4. *Rafael Villarreal Pacheco:* Applications of Geographic Information Systems as an analytical and visualization tool for mass real estate valuation: a case study of Fontibon District, Bogota, Columbia (2009).
5. *Siri Oestreich Waage:* a case study of route solving for oversized transport: The use of GIS functionalities in transport of transformers, as part of maintaining a reliable power infrastructure (2010).
6. *Edgar Pimiento:* Shallow landslide susceptibility – Modelling and validation (2010).
7. *Martina Schäfer:* Near real-time mapping of floodwater mosquito breeding sites using aerial photographs (2010).
8. *August Pieter van Waarden-Nagel:* Land use evaluation to assess the outcome of the programme of rehabilitation measures for the river Rhine in the Netherlands (2010).
9. *Samira Muhammad:* Development and implementation of air quality data mart for Ontario, Canada: A case study of air quality in Ontario using OLAP tool. (2010).
10. *Fredros Oketch Okumu*: Using remotely sensed data to explore spatial and temporal relationships between photosynthetic productivity of vegetation and malaria transmission intensities in selected parts of Africa (2011).
11. *Svajunas Plunge:* Advanced decision support methods for solving diffuse water pollution problems (2011).
12. *Jonathan Higgins:* Monitoring urban growth in greater Lagos: A case study using GIS to monitor the urban growth of Lagos 1990 - 2008 and produce future growth prospects for the city (2011).
13. *Mårten Karlberg:* Mobile Map Client API: Design and Implementation for Android (2011).
14. *Jeanette McBride:* Mapping Chicago area urban tree canopy using color infrared imagery (2011).
15. *Andrew Farina:* Exploring the relationship between land surface temperature and vegetation abundance for urban heat island mitigation in Seville, Spain (2011).
16. *David Kanyari*: Nairobi City Journey Planner: An online and a Mobile Application (2011).

17. *Laura V. Drews:* Multi-criteria GIS analysis for siting of small wind power plants - A case study from Berlin (2012).
18. *Qaisar Nadeem:* Best living neighborhood in the city - A GIS based multi criteria evaluation of ArRiyadh City (2012).
19. *Ahmed Mohamed El Saeid Mustafa:* Development of a photo voltaic building rooftop integration analysis tool for GIS for Dokki District, Cairo, Egypt (2012).
20. *Daniel Patrick Taylor*: Eastern Oyster Aquaculture: Estuarine Remediation via Site Suitability and Spatially Explicit Carrying Capacity Modeling in Virginia's Chesapeake Bay (2013).
21. *Angeleta Oveta Wilson:* A Participatory GIS approach to *unearthing* Manchester's Cultural Heritage '*gold mine*' (2013).
22. *Ola Svensson:* Visibility and Tholos Tombs in the Messenian Landscape: A Comparative Case Study of the Pylian Hinterlands and the Soulima Valley (2013).
23. *Monika Ogden:* Land use impact on water quality in two river systems in South Africa (2013).
24. *Stefan Rova:* A GIS based approach assessing phosphorus load impact on Lake Flaten in Salem, Sweden (2013).
25. *Yann Buhot:* Analysis of the history of landscape changes over a period of 200 years. How can we predict past landscape pattern scenario and the impact on habitat diversity? (2013).
26. *Christina Fotiou:* Evaluating habitat suitability and spectral heterogeneity models to predict weed species presence (2014).
27. *Inese Linuza:* Accuracy Assessment in Glacier Change Analysis (2014).
28. *Agnieszka Griffin:* Domestic energy consumption and social living standards: a GIS analysis within the Greater London Authority area (2014).
29. *Brynja Guðmundsdóttir:* Detection of potential arable land with remote sensing and GIS - A Case Study for Kjósarhreppur (2014).
30. *Oleksandr Nekrasov:* Processing of MODIS Vegetation Indices for analysis of agricultural droughts in the southern Ukraine between the years 2000-2012 (2014).
31. *Sarah Tressel:* Recommendations for a polar Earth science portal in the context of Arctic Spatial Data Infrastructure (2014).
32. *Caroline Gevaert:* Combining Hyperspectral UAV and Multispectral Formosat-2 Imagery for Precision Agriculture Applications (2014).
33. *Salem Jamal-Uddeen:* Using GeoTools to implement the multi-criteria evaluation analysis - weighted linear combination model (2014).
34. *Samanah Seyedi-Shandiz:* Schematic representation of geographical railway network at the Swedish Transport Administration (2014).
35. *Kazi Masel Ullah:* Urban Land-use planning using Geographical Information System and analytical hierarchy process: case study Dhaka City (2014).
36. *Alexia Chang-Wailing Spitteler:* Development of a web application based on MCDA and GIS for the decision support of river and floodplain rehabilitation projects (2014).
37. *Alessandro De Martino:* Geographic accessibility analysis and evaluation of potential changes to the public transportation system in the City of Milan (2014).
38. *Alireza Mollasalehi:* GIS Based Modelling for Fuel Reduction Using Controlled Burn in Australia. Case Study: Logan City, QLD (2015).

39. *Negin A. Sanati:* Chronic Kidney Disease Mortality in Costa Rica; Geographical Distribution, Spatial Analysis and Non-traditional Risk Factors (2015).
40. *Karen McIntyre:* Benthic mapping of the Bluefields Bay fish sanctuary, Jamaica (2015).
41. *Kees van Duijvendijk:* Feasibility of a low-cost weather sensor network for agricultural purposes: A preliminary assessment (2015).
42. *Sebastian Andersson Hylander:* Evaluation of cultural ecosystem services using GIS (2015).
43. *Deborah Bowyer:* Measuring Urban Growth, Urban Form and Accessibility as Indicators of Urban Sprawl in Hamilton, New Zealand (2015).
44. *Stefan Arvidsson:* Relationship between tree species composition and phenology extracted from satellite data in Swedish forests (2015).
45. *Damián Giménez Cruz*: GIS-based optimal localisation of beekeeping in rural Kenya (2016).
46. *Alejandra Narváez Vallejo:* Can the introduction of the topographic indices in LPJ-GUESS improve the spatial representation of environmental variables? (2016).
47. *Anna Lundgren:* Development of a method for mapping the highest coastline in Sweden using breaklines extracted from high resolution digital elevation models (2016).
48. *Oluwatomi Esther Adejoro:* Does location also matter? A spatial analysis of social achievements of young South Australians (2016).
49. *Hristo Dobrev Tomov:* Automated temporal NDVI analysis over the Middle East for the period 1982 - 2010 (2016).
50. *Vincent Muller:* Impact of Security Context on Mobile Clinic Activities A GIS Multi Criteria Evaluation based on an MSF Humanitarian Mission in Cameroon (2016).
51. *Gezahagn Negash Seboka:* Spatial Assessment of NDVI as an Indicator of Desertification in Ethiopia using Remote Sensing and GIS (2016).
52. *Holly Buhler:* Evaluation of Interfacility Medical Transport Journey Times in Southeastern British Columbia. (2016).
53. *Lars Ole Grottenberg*: Assessing the ability to share spatial data between emergency management organisations in the High North (2016).
54. *Sean Grant:* The Right Tree in the Right Place: Using GIS to Maximize the Net Benefits from Urban Forests (2016).
55. *Irshad Jamal:* Multi-Criteria GIS Analysis for School Site Selection in Gorno-Badakhshan Autonomous Oblast, Tajikistan (2016).
56. *Fulgencio Sanmartín:* Wisdom-volkano: A novel tool based on open GIS and time-series visualization to analyse and share volcanic data (2016).
57. *Nezha Acil:* Remote sensing-based monitoring of snow cover dynamics and its influence on vegetation growth in the Middle Atlas Mountains (2016).
58. *Julia Hjalmarsson:* A Weighty Issue: Estimation of Fire Size with Geographically Weighted Logistic Regression (2016).
59. *Mathewos Tamiru Amato:* Using multi-criteria evaluation and GIS for chronic food and nutrition insecurity indicators analysis in Ethiopia (2016).
60. *Karim Alaa El Din Mohamed Soliman El Attar:* Bicycling Suitability in Downtown, Cairo, Egypt (2016).

61. *Gilbert Akol Echelai:* Asset Management: Integrating GIS as a Decision Support Tool in Meter Management in National Water and Sewerage Corporation (2016).
62. *Terje Slinning:* Analytic comparison of multibeam echo soundings (2016).
63. *Gréta Hlín Sveinsdóttir:* GIS-based MCDA for decision support: A framework for wind farm siting in Iceland (2017).
64. *Jonas Sjögren:* Consequences of a flood in Kristianstad, Sweden: A GIS-based analysis of impacts on important societal functions (2017).
65. *Nadine Raska:* 3D geologic subsurface modelling within the Mackenzie Plain, Northwest Territories, Canada (2017).
66. *Panagiotis Symeonidis*: Study of spatial and temporal variation of atmospheric optical parameters and their relation with PM 2.5 concentration over Europe using GIS technologies (2017).
67. *Michaela Bobeck:* A GIS-based Multi-Criteria Decision Analysis of Wind Farm Site Suitability in New South Wales, Australia, from a Sustainable Development Perspective (2017).
68. *Raghdaa Eissa*: Developing a GIS Model for the Assessment of Outdoor Recreational Facilities in New Cities Case Study: Tenth of Ramadan City, Egypt (2017).
69. *Zahra Khais Shahid*: Biofuel plantations and isoprene emissions in Svea and Götaland (2017).
70. *Mirza Amir Liaquat Baig*: Using geographical information systems in epidemiology: Mapping and analyzing occurrence of diarrhea in urban - residential area of Islamabad, Pakistan (2017).
71. *Joakim Jörwall*: Quantitative model of Present and Future well-being in the EU-28: A spatial Multi-Criteria Evaluation of socioeconomic and climatic comfort factors (2017).
72. *Elin Haettner*: Energy Poverty in the Dublin Region: Modelling Geographies of Risk (2017).
73. *Harry Eriksson*: Geochemistry of stream plants and its statistical relations to soil- and bedrock geology, slope directions and till geochemistry. A GIS-analysis of small catchments in northern Sweden (2017).
74. *Daniel Gardevärn:* PPGIS and Public meetings – An evaluation of public participation methods for urban planning (2017).
75. *Kim Friberg:* Sensitivity Analysis and Calibration of Multi Energy Balance Land Surface Model Parameters (2017).
76. *Viktor Svanerud:* Taking the bus to the park? A study of accessibility to green areas in Gothenburg through different modes of transport (2017).
77. *Lisa-Gaye Greene*: Deadly Designs: The Impact of Road Design on Road Crash Patterns along Jamaica's North Coast Highway (2017).
78. *Katarina Jemec Parker*: Spatial and temporal analysis of fecal indicator bacteria concentrations in beach water in San Diego, California (2017).
79. *Angela Kabiru*: An Exploratory Study of Middle Stone Age and Later Stone Age Site Locations in Kenya's Central Rift Valley Using Landscape Analysis: A GIS Approach (2017).
80. *Kristean Björkmann*: Subjective Well-Being and Environment: A GIS-Based Analysis (2018).
81. *Williams Erhunmonmen Ojo*: Measuring spatial accessibility to healthcare for people living with HIV-AIDS in southern Nigeria (2018).

82. *Daniel Assefa*: Developing Data Extraction and Dynamic Data Visualization (Styling) Modules for Web GIS Risk Assessment System (WGRAS). (2018).
83. *Adela Nistora*: Inundation scenarios in a changing climate: assessing potential impacts of sea-level rise on the coast of South-East England (2018).
84. *Marc Seliger*: Thirsty landscapes - Investigating growing irrigation water consumption and potential conservation measures within Utah's largest master-planned community: Daybreak (2018).
85. *Luka Jovičić*: Spatial Data Harmonisation in Regional Context in Accordance with INSPIRE Implementing Rules (2018).
86. *Christina Kourdounouli*: Analysis of Urban Ecosystem Condition Indicators for the Large Urban Zones and City Cores in EU (2018).
87. *Jeremy Azzopardi*: Effect of distance measures and feature representations on distance-based accessibility measures (2018).
88. *Patrick Kabatha*: An open source web GIS tool for analysis and visualization of elephant GPS telemetry data, alongside environmental and anthropogenic variables (2018).
89. *Richard Alphonce Giliba*: Effects of Climate Change on Potential Geographical Distribution of Prunus africana (African cherry) in the Eastern Arc Mountain Forests of Tanzania (2018).
90. *Eiður Kristinn Eiðsson*: Transformation and linking of authoritative multi-scale geodata for the Semantic Web: A case study of Swedish national building data sets (2018).
91. *Niamh Harty*: HOP!: a PGIS and citizen science approach to monitoring the condition of upland paths (2018).
92. *José Estuardo Jara Alvear*: Solar photovoltaic potential to complement hydropower in Ecuador: A GIS-based framework of analysis (2018).
93. *Brendan O'Neill*: Multicriteria Site Suitability for Algal Biofuel Production Facilities (2018).
94. *Roman Spataru*: Spatial-temporal GIS analysis in public health – a case study of polio disease (2018).
95. *Alicja Miodońska*: Assessing evolution of ice caps in Suðurland, Iceland, in years 1986 - 2014, using multispectral satellite imagery (2019).
96. *Dennis Lindell Schettini*: A Spatial Analysis of Homicide Crime's Distribution and Association with Deprivation in Stockholm Between 2010-2017 (2019).
97. *Damiano Vesentini*: The Po Delta Biosphere Reserve: Management challenges and priorities deriving from anthropogenic pressure and sea level rise (2019).
98. *Emilie Arnesten*: Impacts of future sea level rise and high water on roads, railways and environmental objects: a GIS analysis of the potential effects of increasing sea levels and highest projected high water in Scania, Sweden (2019).
99. *Syed Muhammad Amir Raza*: Comparison of geospatial support in RDF stores: Evaluation for ICOS Carbon Portal metadata (2019).
100. *Hemin Tofiq*: Investigating the accuracy of Digital Elevation Models from UAV images in areas with low contrast: A sandy beach as a case study (2019).
101. *Evangelos Vafeiadis*: Exploring the distribution of accessibility by public transport using spatial analysis. A case study for retail concentrations and public hospitals in Athens (2019).

102. *Milan Sekulic*: Multi-Criteria GIS modelling for optimal alignment of roadway by-passes in the Tlokweng Planning Area, Botswana (2019).
103. *Ingrid Piirisaar*: A multi-criteria GIS analysis for siting of utility-scale photovoltaic solar plants in county Kilkenny, Ireland (2019).
104. *Nigel Fox*: Plant phenology and climate change: possible effect on the onset of various wild plant species' first flowering day in the UK (2019).
105. *Gunnar Hesch*: Linking conflict events and cropland development in Afghanistan, 2001 to 2011, using MODIS land cover data and Uppsala Conflict Data Programme (2019).
106. *Elijah Njoku*: Analysis of spatial-temporal pattern of Land Surface Temperature (LST) due to NDVI and elevation in Ilorin, Nigeria (2019).
107. *Katalin Bunyevácz*: Development of a GIS methodology to evaluate informal urban green areas for inclusion in a community governance program (2019).
108. *Paul dos Santos*: Automating synthetic trip data generation for an agent-based simulation of urban mobility (2019).
109. *Robert O' Dwyer*: Land cover changes in Southern Sweden from the mid-Holocene to present day: Insights for ecosystem service assessments (2019).
110. *Daniel Klingmyr*: Global scale patterns and trends in tropospheric NO_2 concentrations (2019).